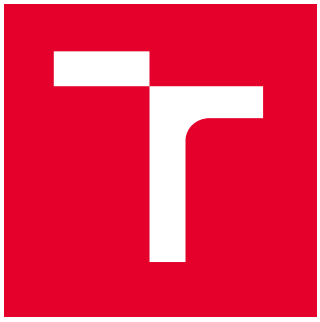

BRNO UNIVERSITY OF TECHNOLOGY

VYSOKÉ UČENÍ TECHNICKÉ V BRNĚ

FACULTY OF ELECTRICAL ENGINEERING AND COMMUNICATION

FAKULTA ELEKTROTECHNIKY
A KOMUNIKAČNÍCH TECHNOLOGIÍ

DEPARTMENT OF BIOMEDICAL ENGINEERING

ÚSTAV BIOMEDICÍNSKÉHO INŽENÝRSTVÍ

INTRACRANIAL ANEURYSM DETECTION IN TOF-MRI DATA

DETEKCE INTRAKRANIÁLNÍCH ANEURYSMAT V TOF-MRI DATECH

MASTER'S THESIS
DIPLOMOVÁ PRÁCE

AUTHOR
AUTOR PRÁCE

Bc. Jan Vývoda

SUPERVISOR
VEDOUCÍ PRÁCE

Ing. Roman Jakubíček, Ph.D.

BRNO 2022

BRNO UNIVERSITY OF TECHNOLOGY
FACULTY OF ELECTRICAL ENGINEERING AND COMMUNICATION

Master's Thesis

Master's study program **Biomedical Engineering and Bioinformatics**

Department of Biomedical Engineering

Student: Bc. Jan Vývoda ***ID:*** 203692

Year of study: 2 ***Academic year:*** 2021/22

TITLE OF THESIS:

Intracranial aneurysm detection in TOF-MRI data

INSTRUCTION:

1) Get acquainted with the issue of intracranial aneurysms, their diagnosis, and the motivation for automatic detection, including the study of the possibilities of angiography and the use of TOF-MRI imaging modality. 2) Develop a survey of available detection methods, focusing on machine learning methods, including examples of already published solutions. 3) Ensure the availability of the TOF-MRI database in the "ADAM" competition, familiarize yourself with the structure, format and data types for retrieval and subsequent work. Based on the search, propose a detection methodology, including a discussion of possible preprocessing and postprocessing. 4) Implement the proposed detection approach in the chosen programming environment. Perform an initial success analysis on a test database. 5) Perform a more detailed evaluation of the success of the proposed approach and propose and implement appropriate modifications or different approaches. Analyze the influence of parameters and the correctness of the design as part of the validation. 6) Appropriately present and discuss the results obtained, the possible applications and the aneurysm detection problems encountered.

RECOMMENDED LITERATURE:

[1] TIMMINS, Kimberley, et al., 2020. Intracranial Aneurysm Detection and Segmentation Challenge 2020. B.m.: Zenodo. Doi:10.5281/zenodo.3715848

[2] UEDA, Daiju, et al., 2019. Deep learning for MR angiography: Automated detection of cerebral aneurysms. Radiology [online]. 290(1), 187–194. ISSN 15271315. Doi:10.1148/radiol.2018180901

Date of project specification: 7.2.2022 ***Deadline for submission:*** 20.5.2022

Supervisor: Ing. Roman Jakubíček, Ph.D.

prof. Ing. Ivo Provazník, Ph.D.
Chair of study program board

ABSTRACT

The thesis contains a theoretical review of information about intracranial aneurysms, their diagnosis and therapy. It also summarizes the methods of object detection by both classical and machine learning methods and includes a brief description of some methods of intracranial aneurysm detection. In the practical part, several proposed approaches for segmentation and detection of these aneurysms using U-net neural network are evaluated and compared.

KEYWORDS

Intracranial aneurysm, aneurysm, machine learning, detection, magnetic resonance, U-net

ABSTRAKT

Práce obsahuje teoretický přehled informací o intrakraniálních aneurysmatech, jejich diagnostice a terapii. Dále shrnuje metody detekce objektů jak klasickými metodami, tak metodami strojového učení a také obsahuje stručný popis některých metod detekce intrakraniálních aneurysmat. V praktické části je vyhodnoceno a porovnáno několik navrhnutých postupů segmentace a detekce těchto aneurysmat pomocí neuronové sítě U-net.

KLÍČOVÁ SLOVA

Intrakraniální aneurysma, aneurysma, strojové učení, detekce, magnetické rezonance, U-net

ROZŠÍŘENÝ ABSTRAKT

Úvod

Detekce intrakraniálních aneurysmat (IA) je velmi důležitá, protože tento problém postihuje 5-10 % populace. V mnoha případech je přítomnost aneurysmatu zjištěna až při subarachnoidálním krvácení (SAH) jako následek ruptury tohoto IA. Úmrtnost na SAH způsobenou prasklým aneurysmatem se pohybuje mezi 23 % a 51 % a poměrně velké procento lidí zůstává s trvalými následky. Proto je nutné zaměřit se na detekci IA i před jejich prasknutím, což je velmi složitý a náročný úkol. K diagnostice se používá mnoho metod, ale i tak je nalezení aneurysmatu na těchto snímcích obtížné a lékaři musí být velmi zkušení. Proto je důležité zaměřit se na vytvoření metody pro detekci aneurysmat, která by lékařům práci zjednodušila a urychlila.

První částí této magisterské práce je literární rešerše, která se zabývá problematikou intrakraniálních aneurysmat, popisem anatomie a fyziologie cévního systému mozku. Zabývá se také diagnostikou a léčbou intrakraniálních aneurysmat. Zmiňuje se také o vyšetřovacích metodách a o metodách detekce objektů. Ty jsou rozděleny na tradiční metody a metody strojového učení. U metod strojového učení je zmíněna také segmentace pomocí U-netu, která je dále využívána v praktické části.

Praktická část této magisterské práce se zabývá detekcí intrakraniálních aneurysmat a subarachnoidálního krvácení. K detekci je využita neuronová síť U-net, která snímek segmentuje. V takto segmentovaném snímku je pak nelezen střed segmentů, jako pozice aneurysmat a SAH. Protože je samotná detekce velmi závislá na kvalitě segmentace, je navrženo několik segmentačních přístupů. Jedná se o segmentaci pomocí celých snímků (řezů), segmentaci obrazu po částech a také 3D segmentaci. Protože při segmentaci vzniká velké množství falešně pozitivních segmentů, byly navrženy metody na jejich eliminaci, s cílem zlepšit detekci. Detekce se provádí výpočtem centroidů vytvořených segmentů z obrazových (geometrických) momentů získaných z jejich kontur.

Popis řešení

V této práci byly používány NIfTI data z time-of-flight magnetické rezonance. Data byla poskytnuta od autorů projektu ADAM (Aneurysm Detection and Segmentation). Soubor dat obsahuje údaje o 113 případech. Jedná se o 23 unikátních pacientů s aneurysmaty a SAH, 35 základních a 35 následných vyšetření s aneurysmatem a SAH a také 20 zdravých pacientů. Součástí dat byly také anotace v podobě

binární masky. Všechny snímky byly již předzpracovány pomocí korekce pro úpravu zkresleného pole. Pro další zpracování a snížení výpočetní náročnosti byla použita stejná velikost voxelu pro všechny snímky s délkou hrany 1 mm. Data byla rovněž normalizována na rozsah od 0 do 1 s využitím maxima a minima v obraze.

V rámci přípravy dat bylo dále všech 113 vyšetření náhodně rozděleno na 84 trénovacích a 29 validačních. Dále pro snazší práci s daty byl vždy vytvořen seznam cest k danému vyšetření a index vybraného řezu. Pro trénování sítě bylo vybráno jen několik řezů tak, aby do sítě nevstupovalo příliš mnoho řezů bez aneurysmat.

Všechny navržené přístupy jsou založené na segmentaci pomocí U-netu. První přístup segmentuje celý řez najednou, ale kvůli velkému poměru mezi počtem pixelů pozadí a pixelů aneurysmat je potřeba využít loss funkci, která kompenzuje pozitivní odpověď. V tomto případě byla použita průměrná hodnota Binární vzájemné entropie a Dice funkce. Pro optimalizaci byl použit algoritmus Adam. Síť byla učena 160 epoch s počátečním učícím krokem $1e^{-4}$, který byl po prvních 40-ti epochách snížen o 0.1.

Druhý přístup je podobný tomu prvnímu. Využívá stejný U-net, ale je doplněn následným krokem eliminace falešně pozitivních segmentů. Pro tuto eliminaci byly využity dvě metody. První metoda je založena na eliminaci pomocí malé konvoluční neuronové sítě, která klasifikuje, zda se jedná o falešný segment, nebo aneurysma. Pakliže jde o falešný segment, tak je vyplněn černými pixely. Druhá metoda je založena na opakované segmentaci jednoho snímku pod různými úhly (úhly v rozmezí $-2°$ až $+2°$). Touto metodou dochází k eliminaci převážně malých segmentů.

Třetí přístup opět řeší velký počet pixelů pozadí. Hlavní myšlenkou tohoto přístupu je rozdělení řezu do několika částí, segmentace těchto částí a zpětné poskládání řezu. Tento přístup nemohl být použit pro učení sítě, jelikož by do ní vstupovalo příliš mnoho prázdných snímků. Proto byla použita funkce na vytvoření náhodných výřezů v okolí aneurysmat. Takto do sítě vstupovali převážně snímky s aneurysmaty a několik snímků bez nich. Pro tento U-net byla využita stejná optimalizace a loss funkce, jako u prvního přístupu. Pouze zde byla snížena váha pozitivní odpovědi. Síť byla učena 165 epoch s počátečním učícím krokem $1e^{-4}$, který byl po prvních 60-ti epochách snížen o 0.1.

Poslední přístup se věnuje segmentaci a detekci aneurysmat v 3D prostoru. Kvůli tomu byla upravena architektura sítě nahrazením 2D konvolučních a poolingových vrstev za 3D vrstvy. Opět je zde použita stejná optimalizace a kombinace loss funkcí. Tento U-net segmentuje 3D kostky o velikosti $40 \times 40 \times 32$, tedy musí dojít k rozdělení původních dat na tyto kostky a k následnému poskládání zpět do původní podoby. Učení probíhalo 125 epoch s počátečním učícím krokem $1e^{-4}$, který byl po prvních 45-ti epochách snížen o 0.1.

Vyhodnocení

K vyhodnocení výsledků bylo vybráno několik statistických metrik. Pro segmentační problém byly vybrány Dice koeficient, Precision, Recall a Pozitivní prediktivní hodnota (PPV). K vyhodnocení přesnosti detekce bylo využito Senzitivity a Manhattanské vzdálenosti centroidů reálných aneurysmat a získaných segmentů. V práci bylo navrženo několik segmentačních přístupů, jelikož kvalita detekce se odvíjí právě od kvality segmentace.

Jako nejlepší segmentační přístup se jeví, na základě výsledků, segmentace celých řezů s eliminací pomocí průniku segmentovaných snímků. Dice koeficient tohoto přístupu dosáhl hodnoty 0.90, pozitivní prediktivní hodnota pak hodnoty 0.84, což znamená, že se zde nevyskytuje příliš velké množství falešně pozitivních segmentů. Z pohledu detekce ale tato metoda není až tak úspěšná, jelikož Senzitivita dosahuje pouze hodnoty 0.60, tedy poměrně velké množství aneurysmat nebylo detekováno.

Naopak přístup využívající segmentace řezů po částech s eliminací FP segmentů nedosahuje příliš dobrých hodnot Dice koeficientu, ale Senzitivita zde šahá až na hodnotu 0.76. Je zde tedy detekováno více aneurysmat, avšak podle PPV se zde vyskytuje také hodně falešně pozitivních segmentů, a proto je velmi těžké rozhodnout, který z těchto přístupů má kvalitnější detekci. Pokud by došlo k lepší eliminaci falešně pozitivních segmentů v přístupu segmentace řezů po částech, pak by výsledná detekce překonala přístup s využitím celých snímků.

Přístup využívající 3D segmentaci nebyl příliš úspěšný a to hlavně kvůli vytváření velkého počtu FP segmentů při segmentaci. Velkým problémem byla chybná segmentace v oblastech cév a některých struktur, které svými vlastnostmi mohly připomínat aneurysma, či subarachnoidální krvácení. Kvůli vysokému počtu falešně pozitivních segmentů sice dosáhl tento přístup nízkých hodnot Manhattanské vzdálenosti, avšak zároveň tento problém snižuje úspěšnost detekce.

VÝVODA, Jan. *Intracranial aneurysm detection in TOF-MRI data*. Brno: Brno University of Technology, Faculty of Electrical Engineering and Communication, Department of Biomedical Engineering, 2022, 59 p. Master's Thesis. Advised by Ing. Roman Jakubíček, Ph.D.

Author's Declaration

Author:	Bc. Jan Vývoda
Author's ID:	203692
Paper type:	Master's Thesis
Academic year:	2021/22
Topic:	Intracranial aneurysm detection in TOF-MRI data

I declare that I have written this paper independently, under the guidance of the advisor and using exclusively the technical references and other sources of information cited in the paper and listed in the comprehensive bibliography at the end of the paper.

As the author, I furthermore declare that, with respect to the creation of this paper, I have not infringed any copyright or violated anyone's personal and/or ownership rights. In this context, I am fully aware of the consequences of breaking Regulation § 11 of the Copyright Act No. 121/2000 Coll. of the Czech Republic, as amended, and of any breach of rights related to intellectual property or introduced within amendments to relevant Acts such as the Intellectual Property Act or the Criminal Code, Act No. 40/2009 Coll. of the Czech Republic, Section 2, Head VI, Part 4.

Brno ....

author's signature*

*The author signs only in the printed version.

ACKNOWLEDGEMENT

I would like to thank my thesis advisor, Ing. Roman Jakubíček, Ph.D., for his consultations, very good suggestions and a patience he had with me. I would like to thank the authors Kimberley M. Timmins, Irene C. Van Der Schaaf, Edwin Bennink, et al, for providing the data used in this work, as well.

Contents

List of Figures

List of Tables

Introduction

Detection of intracranial aneurysms (IA) is very important, since it affects 5-10 % of the population [2]. In a lot of cases, the presence of aneurysm is only discovered during subarachnoid haemorrhage (SAH) as a consequence of a rupture of this IA. The mortality of SAH caused by ruptured aneurysm is between 23 % and 51 % and moreover a fairly large percentage of people will remain disabled [28]. Therefore, it is necessary to focus on the detection of IA before they rupture, which is very complex and challenging. Many methods are used for diagnosis, such as digital subtraction angiography (DSA), computed tomography angiography (CTA) or magnetic resonance angiography (MRA). But even so, finding an aneurysm in these images is difficult and the doctors must be very experienced. Therefore, it is important to focus on creating an aneurysm detection algorithm, such as machine learning algorithm, that would support and facilitate the work of doctors.

The first part of the master's thesis describes the theory. It deals with the problem of intracranial aneurysms, description of anatomy and physiology of the vascular system of the brain and the diagnosis and treatment of intracranial aneurysms. It mentions CT angiography, digital subtraction angiography and most of all magnetic resonance imaging and its use in the diagnosis of IAs. Methods of object detection are discussed as well. These are divided into traditional and machine learning methods. In machine learning methods, a U-net segmentation is mentioned, which is further exploited in the practical part.

The practical part of this master's thesis deals with the detection of intracranial aneurysms and subarachnoid haemorrhage using U-net prior segmentation. Since the success rate of detection is highly dependent on the segmentation accuracy, several segmentation methods were proposed. These are segmentation using whole images, segmentation using patches of images and 3D segmentation. Since a large number of false positive segments were generated during segmentation, methods for eliminating these segments were proposed to improve the detection success rate. The detection is performed by calculating the centroids of the obtained segments from the image (geometrical) moments obtained from the contours of these segments.

Based on the results described in the last part of the thesis, the approach using full images followed by elimination of FP segments, and approach using patches of image with elimination seem to be the best. The elimination is done by intersecting several identical images segmented at slightly different angles. It is really hard to determine which one of these approaches was best. First approach mentioned, had very good PPV value of 0.84, but Sensitivity was not as good as in the other approach, whereas the approach using patches of images had worse PPV value, so there was significantly more false positive segments even after the elimination.

1 Intracranial aneurysms

Intracranial aneurysms (IA) are types of lesions that arise from the widening of arteries at the site of their branching in a human brain, resulting in a bulge as shown in figure 1.1b. Some of the aneurysms then lead to rupture and subarachnoid haemorrhage (SAH) with serious consequences. The cause of their formation is still uncleare.[1] If we compare the incidence of SAH with the overall incidence of aneurysms, it is clear that the majority of aneurysms do not rupture, making their detection very challenging. Among the factors that predict whether or not an aneurysm will rupture are the size and location of the aneurysm.[2]

1.1 Anatomy of the vascular system of the brain

Although the weight of the human brain is only a fraction of the weight of a human, it is supplied with up to 15 % of the blood from the resting blood circulation. The brain is supplied by two carotid arteries and two vertebral arteries.[3]

The carotid arteries are then divided into the internal carotid arteries, entering the circle of Willis, which is shown in image 1.1a, and the external carotid arteries, which supply the front of the brain. The vertebral arteries supply the posterior parts of the brain, the spinal cord, cerebellum and brainstem and their connection creates the basilar artery, which is part of the Circle of Willis, also known as the arterial loop. This, often symmetrical, arterial loop is connecting the left and right cerebral hemispheres and the anterior and posterior cerebral circulation.[4] An important finding is that more than half of the cases of intracranial aneurysms are located directly within the circle of Willis and its major branches.[3] [8]

1.2 Physiology of the vascular system of the brain

The human brain has a limited capacity to store the nutrients necessary for its proper function. At the same time, its metabolism is very fast and therefore it is essential that it is constantly supplied with nutrients and oxygen, for which precise regulation of cerebral blood flow is critical. For example, a significant reduction in blood flow results in damage, subsequent unconsciousness and even death.[4]

1.2.1 The importance of partial pressures in the brain

An important aspect of cerebral perfusion is the partial pressure of oxygen (P_aO_2) and especially the partial pressure of carbon dioxide in arterial blood (P_aCO_2).[6] The brain is very sensitive to these partial pressures compared, for example, with

peripheral blood vessels, and changes in these are crucial. With hypercapnia (increase in P_aCO_2), blood flow through the brain increases and conversely, hypocapnia (decrease in P_aCO_2) decreases this flow. This affects the amount of CO_2 in tissue . If there is no oxygen in the body, ventilation is increased and therefore hypocapnia occurs, thus changes in the partial pressures of oxygen and carbon dioxide in arterial blood affect both cerebral blood flow and ventilation.[5]

1.2.2 Brain metabolism

The brain is a highly complex interconnected network that enables communication between brain units. Certain parts of this network contain significantly more connections than others. These parts are called hubs, which have increased metabolism in both the resting and active stages of the brain. Brain metabolism refers to the consumption of glucose by the brain for energy production, primarily by oxidative phosphorylation and by aerobic glycolysis. It can be stated that metabolism varies proportionally with cerebral blood flow.[7]

1.3 Pathology of intracranial aneurysms

Aneurysms can occur in a variety of sizes. They are generally divided into small aneurysms, which are less than 15 mm, large aneurysms are in the range of 15-25 mm, giant aneurysms fall in the range of 25-50 mm, and super giant aneurysms, which are larger than 50 mm, occur as well. Since a large majority of aneurysms encountered in practice fall into the category of small aneurysms, these are further divided into small aneurysms up to 5 mm and medium aneurysms which are 5-15 mm in size.[10]

One of the main causes of intracranial aneurysms is the disruption of the internal elastic lamina, which is either completely absent or present only in small fragments, called Reuterwallt tears.

Various types of cells, such as T lymphocytes, B lymphocytes or macrophages, which can cause inflammation, are often found in the wall of aneurysms. There are a number of factors that contribute to aneurysm rupture. These are, for example, smoking, excessive alcohol consumption, age, family history, etc. The morbidity and mortality is significant in case of ruptured aneurysms, but patients treated with unrupted aneurysms often die within a year after the treatment.[8]

Due to the lack of knowledge of the causes of aneurysm formation, progression and rupture, there is still no non-invasive, safe treatment for aneurysms to this date.[9]

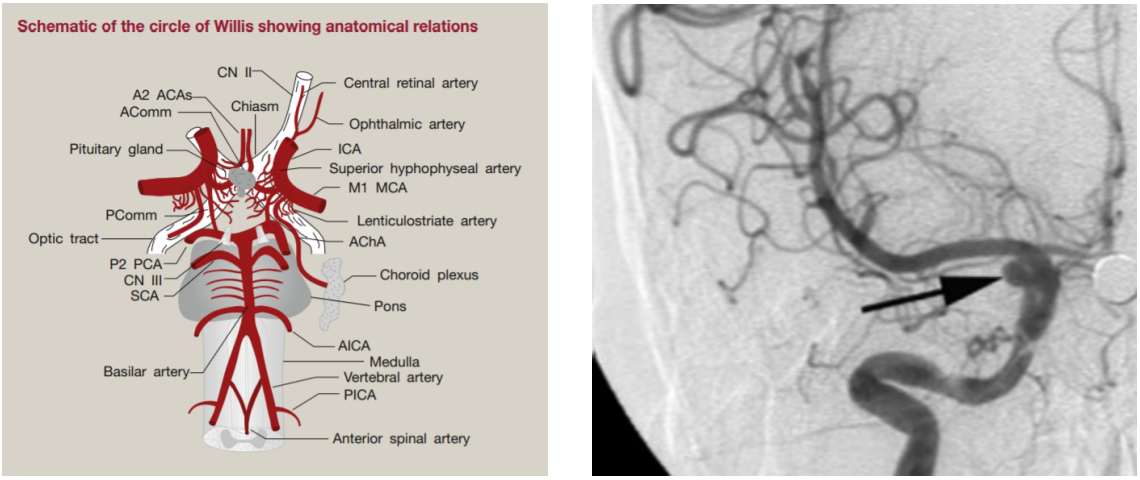

(a) (b)

Fig. 1.1: Image (a) shows the circle of Willis [3]. Figure (b) shows a small aneurysm of the right internal carotid artery [11].

1.4 Diagnosis and treatment of IA

The imaging methods used to examine patients with cerebral aneurysms continue to improve. This gives doctors a better basis for treatment and patient care. However, the examining physician must have extensive knowledge in this area, such as the risks of aneurysm rupture, identification of risk groups and, of course, must be experienced in the imaging technique being used.[10] A large proportion of patients die as a result of haemorrhage, so a rapid detection and evaluation of aneurysms is important.[11]

The digital subtraction angiography (DSA) is a very common and available imaging method, but it is time consuming and invasive. A minimally invasive diagnostic method, which nowadays often replaces the DSA is computed tomography angiography (CTA).[11] Another method used is magnetic resonance angiography (MRA). This is usually used to diagnose patients in whom an aneurysm is already suspected or in patients who have a family history of aneurysms. The most widely used MRI method for aneurysm detection is time-of-flight (TOF) MRI, which provides very good spatial resolution. However, TOF-MRI has disadvantages, such as susceptibility to patient motion.[10] This method is more discussed in chapter 2.2.

1.4.1 Modalities used for the diagnosis of IA

Digital subtraction angiography

Nowadays, digital subtraction angiography (DSA) remains the gold standard in the diagnosis of intracranial aneurysms. Although it is an invasive method, its high resolution and the possibility of creating a three-dimensional image outweigh this disadvantage. However, two-dimensional DSA is commonly used.[16]

DSA is generally used to produce an image that contains only blood vessels in perfect conditions. This is achieved by first taking a conventional X-ray image of the patient. Subsequently, a contrast agent is injected into the patient through a vein to make the blood vessels visible. The contrast agent is administered using ultrasound and the patient is often under local anaesthetic during the procedure. In addition, the conventional X-ray image is subtracted from the contrast image to remove any surrounding tissue, bone or foreign objects that may occure in the patient's body. The resulting image then shows only the blood vessels.[19]

Computed tomography angiography

Computed tomography angiography (CTA) has been used for more than 30 years and its use for the diagnosis of intracranial diseases continues to grow. According to studies, the sensitivity of this method reaches up to 97 % and the specificity even up to 100 %.[16]

CTA differs from a normal CT scan in that a contrast agent is injected into the patient to make the blood vessels visible. Subsequently, single projections are taken, usually at angles of 0-180° with an increment of 1°.[15] Once all projections have been taken, an image can be created, usually using a filtered back projection method.[18]

Magnetic resonance angiography

The main advantage of MRA over the aforementioned DSA and CTA is that the patient is not exposed to radiation during the examination. [15] The MRA technique displays the blood vessels and surrounding tissues with different signal intensities. There are several types of MRA examinations, these are phase contrast MRA, black-blood MRA, time-of-flight MRA, in which it is important that the blood moves faster than the surrounding structures, and the contrast-enhanced MRA technique, where a contrast agent is used. [12] MRA examination is discussed in more detail in the chapter 2.

1.4.2 Treatment and therapy of IA

The main goal of IA treatment is to prevent them from rupturing. Surgical clipping has been used for several years and endovascular embolization is a very frequently used method, but complications such as aneurysm perforation or cerebral ischemia occur. The treatment of unruptured IAs remains controversial as it depends on the condition of the aneurysm. According to the source used, "Unruptured cerebral aneurysms in any location should be considered first for endovascular treatment".

In ruptured IAs, the most common symptom is acute headache resulting from SAH. Endovascular treatment was initially applied only to difficult cases of IAs, where access to the anuerysm was the main problem. Today, thanks to better techniques and approaches, endovascular treatment has become an alternative to surgical treatment. However, there are still some limitations, mainly the size, location of the aneurysm. Thus, there are still cases where surgical intervention is preferred. Nowadays it is exactly the opposite of what it used to be, i.e. in the majority of cases endovascular treatment is used and only in very complex cases surgical treatment is preferred.[13]

2 Magnetic resonance imaging

2.1 General principle of MRI

The magnetic resonance (MR) image is formed by the signal from the nuclei of hydrogen atoms. In the case of hydrogen, we are particularly interested in its proton, which has a specific spin, meaning that the proton rotates on its axis. Such a spinning proton has a angular momentum m and a magnetic moment B.[12]

2.1.1 Physical principle of MR

In magnetic resonance, we expose the hydrogen nucleus to an external magnetic field B_0 and thus achieve alignment of the spins of all hydrogen nuclei with the B_0 field. In addition to directional alignment, they are subject to precession, which is rotation off their axis. The frequency of the precession is given by the so-called Larmor frequency, which is directly proportional to the strength of the external magnetic field B_0.[14] Now, the protons are rotating parallel to the *z-axis* and longitudinal magnetization M_z occurs. Subsequently, an impuls (RF implus), with a frequency in the range of tens to hundreds of Hz, is sent from the transmitting coils which causes the rotating protons to deflect away from the *z-axis* until all the longitudinal magnetization is rotated into the *xy-plane*. At this point, the transverse magnetization M_{xy} is present, which induces a Larmor frequency voltage on the receiving coils. This signal is then further processed. This signal decays rapidly due to spin-lattice and spin-spin interaction. These two interactions then cause T1 and T2 relaxation.[14] [15]

T1 relaxation

The nuclei gradually return to the original position of longitudinal magnetization M_z, which is called longitudinal relaxation as shown in figure 2.1. The nuclei gradually dissipate energy into their surroundings (spin-lattice relaxation) and the time it takes to return to its original position, denoted T1, depends on the intensity B_0.[14]

T2 relaxation

This is a transverse relaxation, which is caused by the spins exchanging excess energy between themselves (spin-spin relaxation) and thus not rotating in phase, but losing this coherence. The parameter T2 is the time constant over which dephasing occurs and is not affected by the intensity of B_0.[14] The T2 relaxation may be seen in figure 2.2.

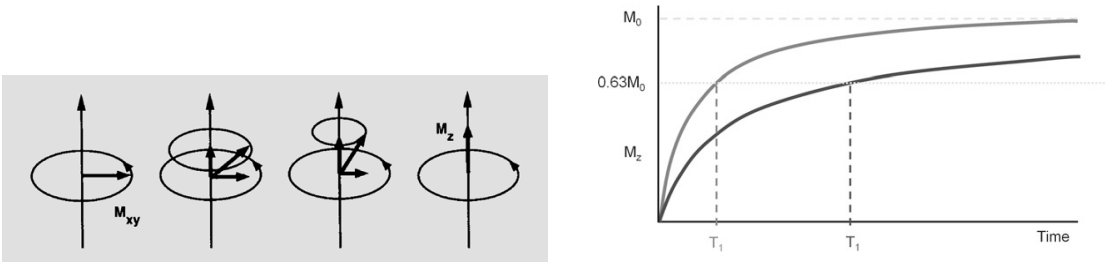

(a) (b)

Fig. 2.1: Image (a) shows the increase of longitudinal magnetization M_z back to its original value. [12] Figure (b) shows that the time constant T1 represents the time for the magnetization M_z to return to 63 % of its original value. The T1 constants for two different tissues are shown.[14]

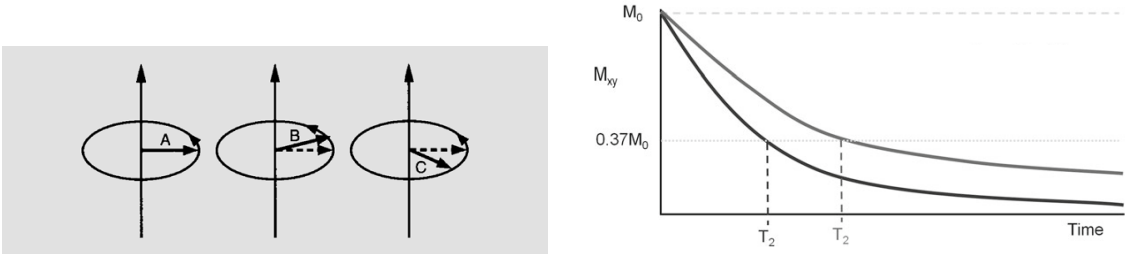

(a) (b)

Fig. 2.2: Image (a) shows how the vectors rotate about the *z-axis* while being in phase with each other.[12] Figure (b) defines that the time constant T2 corresponds to the reduction of the transverse magnetization to 37 % of its original value.[14]

T2* relaxation

The T2* constant tends to be shorter than T2 and is called the decay of free induction, and the T2* effects are due to the effects of additional field inhomogeneities. This can be avoided by using the spin-echo (SE) sequence.[12]

2.1.2 Image creation

As explained earlier, the measured MR signal is produced by the action of an RF pulse on hydrogen protons. However, in order not to excite all the protons at once, we first need to ensure that the external magnetic field is not homogeneous. This is solved by using gradient coils to influence the external magnetic field, so that the field strength varies linearly with position. Thus, each slice has its unique Larmor frequency and thus the RF pulse excites only the protons in a particular slice.

The thickness of the slice is determined by the steepness of the gradient.[15] The most complex task is spatial encoding, which is based on the principle of applying additional gradients that change the magnetic field strength along the y and x axes (the *z-axis* is parallel to the patient axis). Spatial coding is divided into phase and frequency coding. In phase encoding, the gradient in the *y-axis* is altered, causing protons higher in the MR port to increase their precession rate (gain phase) relative to protons lower down. When this gradient is turned off, they return to their original precession rate, but no longer remain in phase.[14] For frequency encoding, the gradient along the *x-axis* is changed. So the precession rate of the protons is changed again, but now along the *x-axis*, and thus the entire frequency spectrum is obtained when the MR signal is detected.[15] So by frequency and phase coding each voxel is identified. To obtain the resulting signal from two dimensions (*x-axis* and *y-axis*), 2D-Fourier transform needs to be used.[12]

Signal contrast of the image

Three parameters mainly affect the appearance of the image. These are the relaxation times T1 and T2 and then the proton density of the tissue. There are two types of images, T1-weighted and T2-weighted.[12]

In the T1-weighted image, the repetition time (TR) indicates the time between two RF pulses in one slice. When the TR is short, then tissues with a short T1 time will give a large signal after the next RF pulse, which will be reflected as a higher intensity in the final image. Tissues with a long T1 time will give a weaker signal (they will be dark in the image). Depending on the length of the TR, we then distinguish between strongly or weakly weighted T1 images.

T2-weighted image is affected by echo time (TE). TE is the time between the application of the RF pulse and the detection of the MR signal. If a suitable TE is used, then tissues with a long T2 time produce a strong signal and are therefore bright in the image, and conversely, tissues with a short T2 time are dark in the image. Again, a distinction is made between strong and weak T2 weighted images, which depends on the length of the TE.

If a short TR and a long TE are used, the signal intensity depends on the proton density of the hydrogen nuclei.[14]

Pulse Sequences

These sequences affect proton excitation, phase encoding, MR signal formation and acquisition, and image formation in general.

The basic sequence is the Spin Echo (SE) sequence. The SE sequence uses a 90° RF pulse for proton excitation. Subsequently, after TE/2 has elapsed, refocusing

occurs using a 180° pulse, resulting in a strong MR signal. Another sequence used is the inversion recovery (IR). In this sequence, a 180° pulse is applied at the beginning. Then it continues as in SE. Usually, a T1-weighted image is acquired using the IR sequence. Another sequence is the short time inversion recovery (STIR) sequence, which is used for fat-suppression. Fluid-attenuated inversion recovery (FLAIR) is used for brain imaging. The gradient echo (GRE) sequence uses a gradient coils instead of RF pulses to produce echo. Because of this, the TR is shortened and thus the image acquisition process is much shorter than in other sequences. The GRE sequence is less susceptible to patient motion and is used in TOF-MR angiography.[12]

2.2 Time of flight Magnetic resonance

The main goal of time-of-flight (TOF) MRI is to highlight blood vessels in the scanned image. TOF magnetic resonance imaging shows the spins of water molecules that are contained in the flowing blood. A blood vessel is imaged brightly if there is a constant supply of additional spins in the imaging plane due to the flowing blood.[14] Very short gradient echo (GRE) sequences are used to excite the water molecules. The spins that are not moving in the imaging plane are highly saturated and therefore the surrounding tissues are depicted darkly in the image. The problem is often slow flowing blood. If the spins remain in a given imaging plane for more than one excitation interval, they become saturated and therefore dark in the image, just as the surrounding tissue is dark. These problems of slow flow can be caused by aneurysms, for example. The problem also exists if the vessel repeatedly returns to the imaging plane. It is not easy to distinguish arteries from veins, as the signal is not dependent on the direction from which the blood comes. This problem can be solved by using presaturation halves before the actual data acquisition.[12] The image that is obtained by TOF-MRI is then gradient-echo T1-weighted.[17]

3 Methods for object detection

3.1 Overview of traditional methods

The detectors used for object detection in the early days were generally based on shapes, edges and components present in the image. Thus, they used to measure some sort of similarity between components, shapes and contours of objects. Initially, these detectors were quite promising, but encountered detection problems with more complex objects.

3.1.1 Wavelet-based approaches

Since 2000, the use of the wavelet transform, which transforms pixels into a set of wavelet coefficients, has become widespread. The Haar wavelet, which is computationally very efficient, has been used most often. One of these early methods is the Viola Jones Detector, which is based on creating features using the wavelet transform with the Haar wavelet just mentioned. Subsequently, only a few useful features are selected using the Adaboost algorithm. The detection itself is then provided by cascade detection, which is able to discard candidates that do not contain the object. However, if the image passes the entire cascade, the object is present and detected. The Viola Jones detector is used for example for face detection.[20]

3.1.2 Histogram of Oriented Gradients Features

Another conventional method is the Histogram of Oriented Gradients (HOG), which works on the principle of a distribution of local gradients of intensity or edge directions. Key points in the image are selected and around them the image is divided into several parts, which can be called cells. In each pixel of these cells, a local histogram of gradient directions or edge orientations is created. Subsequently, we combine all these histograms to create a representation of the image. To improve this feature, an overlapping HOG is used, where cells in the image can overlap and are then merged. A classifier such as Support vector machine (SVM) is often linked to the HOG.[21]

3.1.3 Methods using deformable model

A very good conventional detector is the Deformable part-baset Model (DPM) detector. This method does not just look at the image as a whole, but also the sub-parts of the object that are in the image play a role. The DPM detector consists of a root filter and part filters. The root filter crops the whole object and the sub filters cover

only parts of the object. There is a fully supervised variant, where the root filter is initialized directly in the object, but since annotations are not always available, a weakly supervised DPM is often used, where this filter initialization is done, for example, by a latent SVM.[22]

3.2 Overview of machine learning methods

Machine learning methods have a number of advantages over classical detection methods. For example, that detection capabilities grow exponentially due to deeper architecture, multiple tasks can be optimized simultaneously, and many others.[23] Object detection methods can be divided into three categories.

3.2.1 Two-step methods

This category can be divided into two parts. In the first part, we obtain suggestions of regions in the image where objects might be present. In the second part, the detection part, we obtain the class probabilities of the selected regions and their exact locations. These detectors achieve very good results, but are often not very fast. The first two-step method that combines region search and subsequent detection is R-CNN, which is described in detail in [24]. The main problem with this method, is its speed, due to imperfections in learning and generating the features.[24] Another method is the Spatial Pyramid Pooling Network (SPPNet), which contains a Spatial Pyramid Pooling layer that avoids repeated convolution of features, thus speeding up detection. Problems of R-CNN have been solved by designing Fast R-CNN algorithm, which is able to train object classification and bounding box regression simultaneously, while generating features from the image, as a whole. It also uses a RoI layer for extracting a feature vector layer, where this RoI layer is special case of SPP layer. And then this feature vector is used in the Fully connected layer for object detection.[23] Even so, the speed was not sufficient and therefore the so-called Faster R-CNN was proposed. This method uses a region proposal network (RPN). The RPN shares convolutional layers with the detection network and is able to predict the region and the confidence score of an object at the same time, which greatly speeds up detection and it uses only the last layer of the network for detection itself. Methods such as Mask R-CNN and Feature Pyramids Network (FPN) are based on Faster R-CNN.[24] One other two-step method is R-FCN, which combines the Region of Interest (RoI) layer and a shared fully convolutional subnet that is independent of the RoI subnet.[23]

3.2.2 One-step methods

The second category is One-step methods, which are usually faster, because they design the region and detect the object at the same time, not separately as in Two-step methods.[24] One of the most well-known one-step methods is YOLO, or You Look Only Once, which has been modified over time to be more effective, as well. The first version of YOLO always divided the image into many regions (Usually SxS, where S is the size), instead of using anchors (anchors are pre-defined bounding boxes with different scales that are distributed over the feature map) and then predicted the presence of an object and its class in that region. The classical Mean Square Error (MSE) is used as the Loss function here and YOLO uses fully connected layers for the object detection.[23] The improved version, YOLOv2, solves the problem for the detection of partially overlapped objects. Unsupervised learning directly from the available data is used for bounding box prediction. YOLOv3 then uses binary cross-entropy as a Loss function (YOLOv2 uses Softmax Loss function) to detect multiple objects in a single bounding box and uses a pyramid of features. Another method that falls into this category is the SSD detector, which does not use only one layer to detect the object. SSD uses different sizes of anchor bounding boxes in different depth layers of the network, making it capable of detecting very different objects. Unlike YOLO, SSD uses fully convolutional layers to detect objects. The big drawback with SSD is that it cannot detect small objects well.[24]

3.2.3 Segmentation method

U-net is a convolutional network based method that is not directly used for object detection, but for image segmentation. However, objects can be detected in the segmented image afterwards. U-net plays an important role in the field of medical image analysis. It consists of descending part, bottle-neck and ascending part. In this method the feature vector is created as in the classical convolutional network, but then image is gradually assebled and presented as output of this method.[25] U-net wil be more discussed in section 3.4.

3.3 Methods for IA detection

To present the state-of-the-art methods for IA detection in TOF-MR angiography data, three articles were selected for subsequent discussion.

The first of these articles [28] is entitled ***"Deep Learning for MR Angiography: Automated Detection of Cerebral Aneurysms"***. The dataset was taken at several institutions to avoid overlapping patients. The data were divided

into training, internal test, and external test datasets. The images used for training the algorithm were extended by rotating the original images by 90°, shifting them to the right by 10 %, zooming them by 30 %, and flipping them vertically and horizontally. The untrained ResNet-18 architecture was used for the algorithm. Training of the network was supervised, i.e., the network was given aneurysm cutouts and their annotations. Five-fold cross-validation was used. The hyperparameters were as follows: 100 epochs, Nadam optimizer (learning rate = 0.002, $beta_1 = 0.9$, $beta_2 = 0.999$, epsilon = 1×10^{-8}, schedule decay = 0.004). The output of the network is the probability of aneurysm presence for each cutout. The success rate of the algorithm was as follows: it detected 91 % of the IAs in the internal and 93 % in the external test datasets. Compared with the original radiologists' reports, it improved detection by 4.8 % in the internal test data and 13 % in the external test data.[28]

The second article [29] is entitled ***"Performance of a Deep-Learning Neural Network to Detect Intracranial Aneurysms from3D TOF-MRA Compared to Human Readers"***. As in the first article, images from several institutions were used. Minimal image modifications were performed. The data were resampled to a voxel with an edge size of 0.5 mm and each image was normalized so that the mean intensity was equal to 0 and the standard deviation was 1. Here, the DeepMedic CNN architecture was used to segment the structures in the 3D image data. The parameters of a given model were adjusted based on ground truth and model predictions. Five-fold cross-validation was used here as well, for all datasets, i.e. training, validation and test. According to the results presented in this paper, the algorithm performed very well in detecting IAs > 7 mm in diameter, but did not perform as well as human readers for smaller IAs. The conclusion of this paper is that *CNN is able to detect IAs from TOF-MRA images comparably well to human readers and has great potential to improve IA detection rates.*[29]

The third article [30] is entitled ***"A Two-step Surface-based 3D Deep Learning Pipeline for Segmentation of Intracranial Aneurysms"***. In this study, surface models of the major cerebral arteries were obtained from TOF-MR angiography images using special software. Furthermore, it was necessary to divide the 3D image into smaller fragments in order to perform subsequent segmentation. The size of the fragments was chosen based on the experience of experts. PointNet++ was used to classify the selected fragments, which distinguished whether the fragment was with or without an IA. A soft-max cross entropy loss function was used for training because the number of fragments with IAs was significantly smaller. Fragments classified as those with IA were subsequently entered into the SO-Net segmentation network. The resulting segmentation images were then converted to volume. For validation five-fold cross-validation was applied, where the Dice coefficient was used as the evaluation criterion for the segmentation and sensi-

tivity was used to evaluate the classification network. The mean DSC using five-fold cross validation was 71.79 % and for classification the mean sensitivity was 80.22 %. Thus, the results are quite good, no less a major drawback of this method, as the authors state, is that it requires the support of experts.[30]

3.4 Used methods

As mentioned in the previous section, the U-net consists of 3 parts. Encoding (contracting), bottle-neck and decoding (expanding) parts. This composition is what makes it called a U-net, since it is U-shaped as shown in figure 3.1.

3.4.1 2D U-net

Encoding part

Contracting part is no different from a classical convolutional network in which a feature vector is created. This part consists of two convolutions, with a certain kernel size that the user can set based on the size of the segmented objects. This is followed by a network activation function, usually ReLU, and then a max pooling layer with a certain stride to make the image smaller. In each of these steps we double the number of channels.

Bottle-neck part

The bottle-neck part is used to compress the input data. The output of this part then contains only the useful information that is used in generating the segmented image.[27]

Decoding part

In this method, skip connections are used to crop and map the features in the expanding part. It is important to crop these features, so the dimensions fit and other operations can be performed.[25] The last part of the U-net is the expanding part, where upsampling and subsequent convolution is performed with a 2×2 kernel to reduce the number of channels. Next, a classical convolution is performed with a kernel of the same size as in the encoding part, followed by a ReLU activation function until the output image has the same size as the input image. In the last layer of the U-net, a 1×1 convolution is performed to ensure that the features are mapped to the desired number of classes.[26] With this last convolution Softmax activation function is usually used.

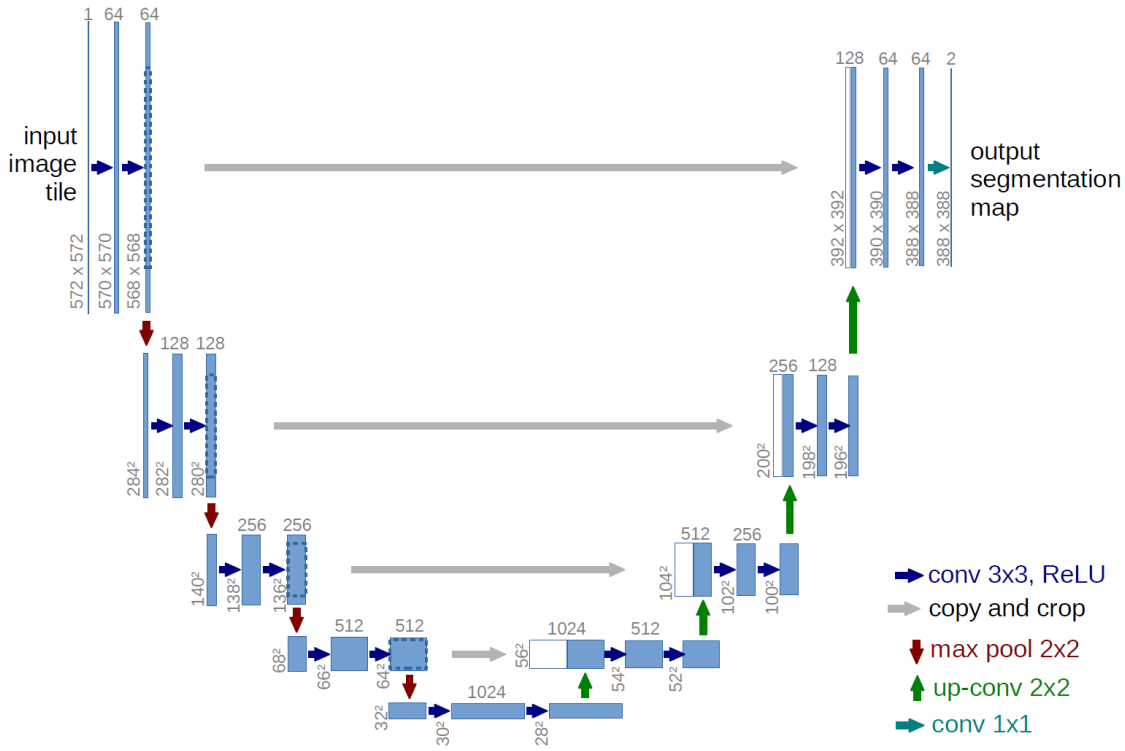

Fig. 3.1: Architecture of the U-net segmentation method taken from [25]. Blue boxes represent feature maps. White boxes are feature maps from skip connections. Each arrow represent an operation as shown in the legend.

3.4.2 3D U-net

Three-dimensional version of U-net is not very different from the 2D version, especially in terms of the U-shaped architecture. There are still the encoding, decoding and bottle-neck part, but the internal components are moved to the third dimension. More precisely, Max-pooling layer and all convolution layers are applied in the third dimension. More structural information is provided for the network due to the third dimension of the data, which could affect the results of segmentation and subsequent detection [31].

4 Design and implementation

Based on the characteristics of the used data several pipelines that are based on segmentation using U-net, were proposed. These pipelines are described in Figure 4.1. These four designs have a common first part of data preparation, which is described in Section 4.2. Segmentation approaches vary a bit and therefore are separately described in Sections below.

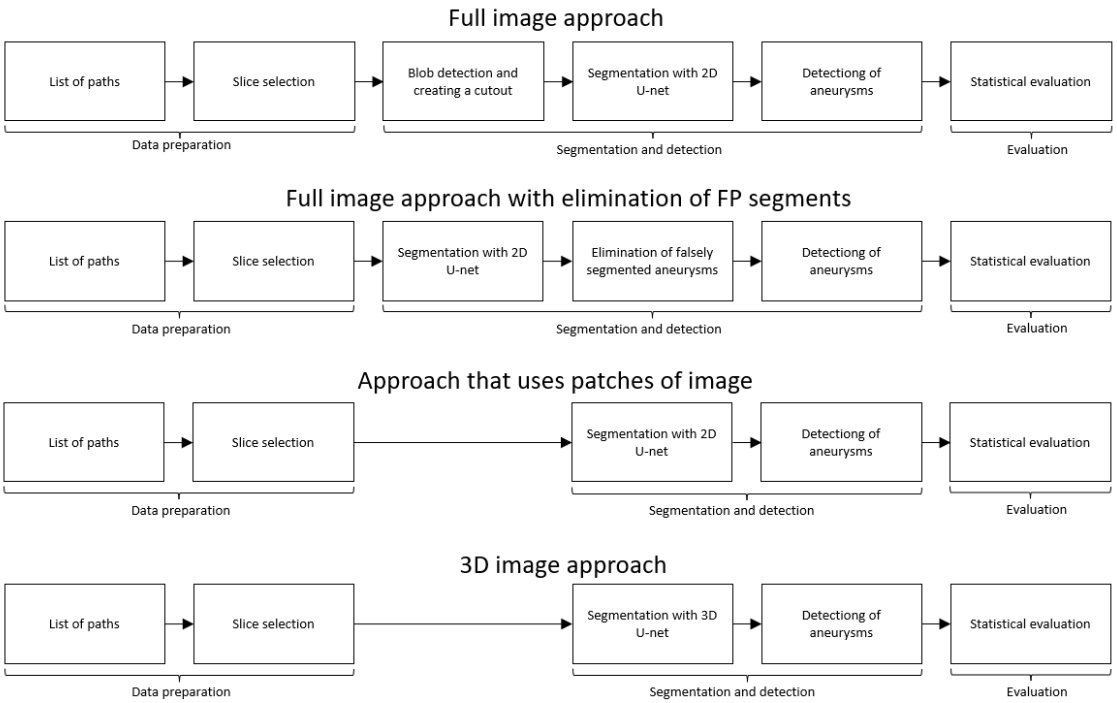

Fig. 4.1: This figure shows proposed pipelines used in this Master's thesis. From top to bottom, these are pipeline of classical U-net segmentation and following detection of aneurysms. Pipeline used for segmentation of image in patches. Pipeline of a classical full image segmentation with additional elimination of FP segments. Block diagram of a 3D segmentation and detection of aneurysms.

4.1 Dataset

The data used in this thesis were provided by the authors Aneurysm Detection and Segmentation (ADAM) challenge. The dataset contains data of 113 cases. There are 23 unique patients with aneurysms and SAH, 35 baseline and 35 follow-up cases with aneurysms and SAH. Then there are also 20 patients who do not have any aneurysms or SAH. The data contain TOF-MRI image and manually created references (masks) of the images and locations of aneurysms in text files. All images

were already preprocessed using correction to adjust the bias field. In this thesis, SAHs are detected as well, because they are part of the provided data.

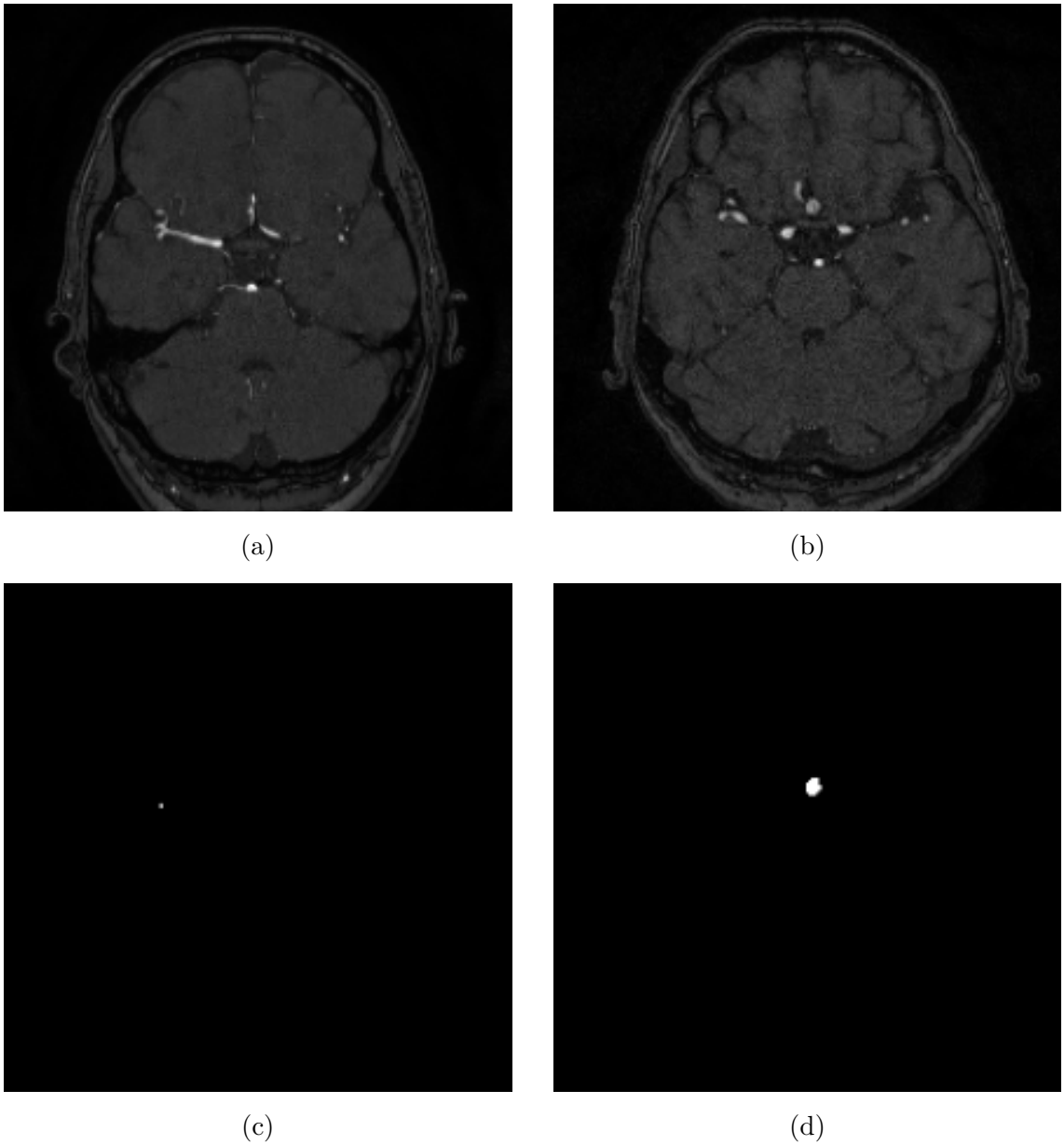

(a) (b)

(c) (d)

Fig. 4.2: This figure shows examples of images and their references. Images (a) and (b) show slices of the TOF-MRI images. Pictures (c) and (d) are their groundtruth masks.

4.2 Data preparation

For further processing and to reduce computational complexity, same voxel size for all images with a 1 mm edge length, was used. Data were also normalized to a

range from 0 to 1 with use of maximum and minimum value of the image. After the normalization the data were saved.

In addition all 113 cases were divided into training and validation datasets. This was done randomly so that there are 84 cases for training and 29 cases for validation.

For easier work with data in the algorithm a list of paths to specific slices was created. The list always contained the path to the patient folder and then the slices that were used for training the network.

To avoid choosing a lot of slices without aneurysms, only a certain number of slices around the center of aneurysm (this information was available in the data) were selected for the training. If the patient did not have any aneurysm, random slices were selected. A function was then used to select the given slices in the dataloader. As these were NIfTI files, the *SimpleITK* library was used to browse through the individual slices in the NIfTI file.

4.3 Proposed approaches of segmentation

The network architecture for all approaches was taken from [25] and therefore corresponds to the Figure 3.1. The key part of the network are two consecutive convolutions with kernel size 3×3 and stride equal to 1 are used for the convolutions. Batch normalization is used to improve training of the network and ReLU activation function is used here. Dimensional reduction is achieved by max-pooling layer with kernel size 2×2 and stride equal to 2. Data augmentation was used in the training process. Specifically, rotating the images by $-35°$ to $35°$ and flipping the images along the X-axis and Y-axis.

At the end of this U-net, there is final 1×1 convolution, that creates a feature map. To binarise the segmented images and evaluate the network, this feature map is converted to a probability map using a sigmoidal function. This is followed by thresholding to get binary image.

This architecture is used in all approaches except the 3D U-net, where all 2D layers (such as convolutional layer, max-pooling layer, batch normalization and up-convolutional layer in the decoding part of the U-net) are replaced with 3D layers.

4.3.1 Full image segmentation

The first approach is based on classical segmentation with use of U-net. Data were prepared as mentioned in Section 4.2 and via dataloader were fed to U-net. Even though a voxel size was initially normalized for the data, the size of the slices varied and therefore had to be resized to size of 200×200 pixels.

Adam optimizer (with β=(0.9, 0.999)) and the average of binary cross entropy with sigmoidal function and Dice coefficient were used for the training process. Weight of the positive responses were set to 150 due to the large ration between the number of black and white pixels. Learning rate was initially set to $1e^{-4}$ and then decreased by 0.1 after 40^{th} epoch. Network was trained for 160 epochs.

4.3.2 Full image segmentation with elimination of false positive segments

This approach is very similar to the 4.3.1, where the same network was used, but with one additional part, which eliminates false positive segments. The main idea was to train another convolutional network (CNN) to perform classification of segments achieved by U-net to improve results of IA detection.

Architecture of this CNN was inspired by MNIST-CNN mentioned in [32] and is shown in Figure 4.3. It consists of three convolutional layers each followed by ReLU activation function and max-pooling layer. At the end there is 1×1 convolutional layer with Softmax.

The principle of this approach is to take the segmented image from U-net and create small patches (with size of 30×30 pixels) around each segment. These patches were created from both, segmented and original TOF-MRI image. There is a third image, that was created by thresholding the TOF-MRI patches and these were fed to the MNIST-CNN with three input channels. As result, segments classified as background were flood-filled with black pixels and therefore eliminated.

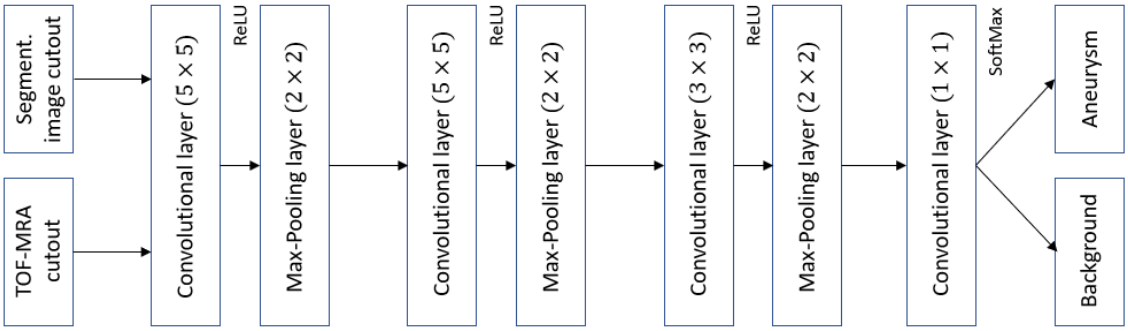

Fig. 4.3: Architecture of modified MNIST-CNN. It consists of three convolutional layers that are followed by ReLU activation function and max-pooling layer. At the end there is final 1×1 convolutional layer with softmax.

Another approach to eliminate false segments is based on segmentation of one image several times, each time with slightly changed angle. Then do an intersection of all these images to eliminate some of the segments. Comparison of these approaches are discussed in Section 5.1.2.

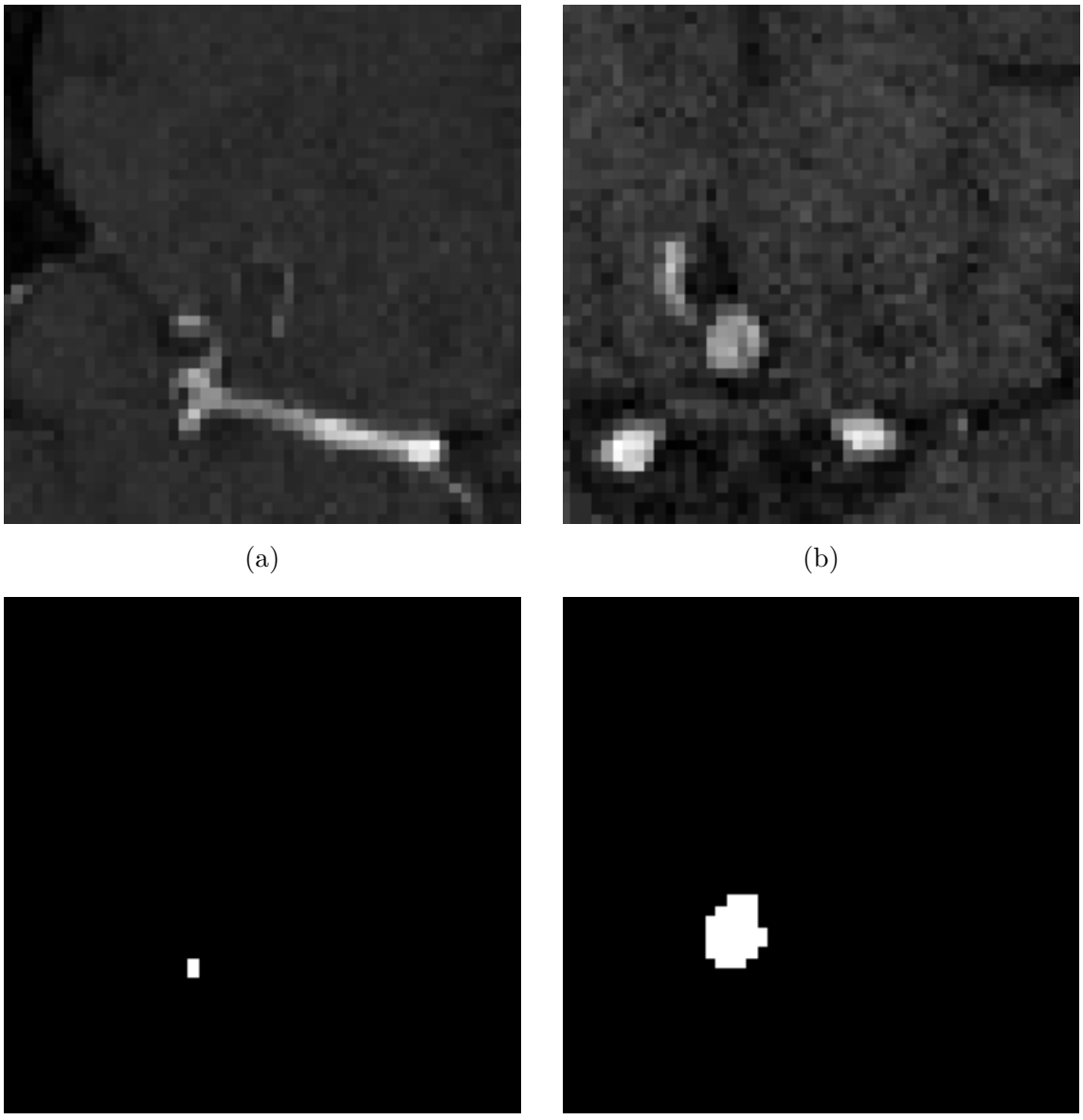

Fig. 4.4: This figure shows random patches used for learning the U-net. Images (a) and (b) show patches of the TOF-MRI images. Pictures (c) and (d) are their patched references.

4.3.3 Segmentation using patches

This approach was introduced to reduce the large ratio between the number of background pixels and aneurysm pixels. In article [33] authors used patches of images to train CNN for segmentation of brain tumors. Their complex segmentation algorithm achieved Dice coefficient 0.90.

The main idea is to divide image into number of patches, perform segmentation

and reassemble the image back into its original form. It would be inappropriate to train the network this way, because there would be a lot of patches containing only the background. Random patches around aneurysms and just a few patches containing only background were used to train the U-net. Size of the patches was set to 50 pixels.

To create these random patches, function with a blob detector (using difference of Gaussian) [36] and contours was used. After finding the aneurysm in the mask a random cropping around it was performed in both, groundtruth mask and original TOF-MRI image. Slices in form of these patches were then fed to the network. In Figure 4.4, there are examples of used random patches.

Same optimizer and combination of loss functions as in 4.3.1 were used here. Weight of the positive response was set to 40. Learning rate was initially set to $1e^{-4}$ and then decreased by 0.1 after 60^{th} epoch. Network was trained for 165 epochs.

4.3.4 3D segmentation

The main idea of this approach is to give the network some additional information of the structure by adding the third dimension. Architecture of the network is quite similar to the classical 2D U-net. The changes consist of replacing 2D layers (convolutional, max-pooling and up-convolutional layers) with 3D layers and feeding the network with 3D images.

Due to the large disproportion of black and white pixels, it is necessary to use small cubes instead of the whole 3D data available. Similar function, that was used in 4.3.3 for creating random patches, was used for training. The final size of the 3D images that were fed to the U-net was $40 \times 40 \times 32$.

Adam was used as an optimizer again and binary cross entropy with sigmoidal function combined with Dice coefficient were used as well. Weight of the positive response was set to 120. Learning rate was initially set to $1e^{-4}$. It was decreased after 45^{th} epoch by 0.1. This 3D U-net was trained for 125 epochs.

4.4 Detection of intracranial aneurysms

After obtaining the segmentation images it was necessary to detect the aneurysms. Since these are binary images it is possible to obtain contours of the segments. Based on these contours, it is possible to retrieve image moments from which centroids of that segments can be calculated according to these formulas:

$$C_x = \frac{M_{10}}{M_{00}}, \tag{4.1}$$

$$C_y = \frac{M_{01}}{M_{00}}, \tag{4.2}$$

where C_x and C_y are coordinates (x, y) of computed centroid and M denotes the Moment.

This detecting method can be than evaluated with Manhattan distance (centroid location), which is described in Section 4.5 below.

4.5 Statistical evaluation

Finally, a statistical evaluation is performed. Precision, Recall and Dice coefficient (DSC) are used for evaluation of the segmentation. These metrics are computed according to the formulas:

$$Precision = \frac{TP}{TP + FP}, \tag{4.3}$$

$$Recall = \frac{TP}{TP + FN}, \tag{4.4}$$

$$DSC = \frac{2TP}{2TP + FP + FN}, \tag{4.5}$$

where TP is number of true positive pixels, FP is number of false positive pixels and FN is number of false negative pixels. The results are discussed in detail in Section 5.

Positive predictive value is also used for evaluation of the segmentation by this formula:

$$PPV = \frac{TP}{TP + FP}, \tag{4.6}$$

where TP is number of true positive segments and FP is number of false positive segments in the segmented image. In case, that there is not an aneurysm in the image and there are not any segments created, the PPV value is equal to 1.

For the detection problem, Manhattan distance between centroids of aneurysms in groundtruth masks and aneurysms in segmented images was chosen as of the metrics. This metric is calculated according to the formula:

$$Man.distance = |x_2 - x_1| + |y_2 - y_1|, \tag{4.7}$$

where y_1, y_2 are coordinates of centroid of the real aneurysm, x_1, x_2 are coordinates of centroid of the segmented aneurysm. For evaluation of 3D U-net, there is a third coordinate z_1 and z_2. The shortest distance values were always selected for the images. It was assumed that the segment with the lowest value was the most accurate estimate.

Sensitivity was used for evaluation of the detection, as well. It presents the probability of correctly detected aneurysm and is computed according to this formula:

$$Sensitivity = \frac{TP}{TP + FN}, \tag{4.8}$$

where TP is number of correctly detected aneurysms, and FN is number of undetected aneurysms.

5 Results and discussion

5.1 Results of individual approaches

In the following Sections, the results of each approach will be discussed and evaluated separately, where first results are obtained on all available validation data (including small and large IAs and SAHs), furthermore the results generated on small aneurysms (size<1mm) only and lastly the results achieved on larger aneurysms and subarachnoid haemorrhages (size>1mm). In the last case, there are also some small aneurysms, as they are present in the same slices.

All Tables presented in section 5.1 have the same structure. They are divided into three columns, where the first column presents results on all available validation data, the second shows results on small aneurysms and the third one shows results achieved on larger aneurysms and SAHs. Values in brackets are standard deviations.

All figures in section 5.1 contain either green or red crosses (dots). Green crosses are centroids of aneurysms in groundtruth masks, red ones represent centroids of segments in segmented images.

5.1.1 Full image segmentation

The results achieved by approach using full image segmentation are presented in Table 5.1. As may be seen, the best performance was achieved in case of large aneurysms and SAHs. The Dice coefficient is in this case very high (Dice = 0.9), which is confirmed by segmentation showed in the first row of Figure 5.1. Positive predictive value is 0.71, thus there are some false positive segments mainly in location of blood vessels (see second row of Figure 5.1). Detection is also most accurate in case of large IAs and SAHs according to the Sensitivity of 0.85, as well as Manhattan distance that is the shortest in this case.

The algorithm achieved good results on all validation data as well. Dice coefficient is only 0.01 smaller than in case of large IAs and SAHs, so the segmentation is on similar level and is shown in the first row of Figure 5.2. The Sensitivity in all validation data is influenced by bad detection of small IAs and therefore reaches values of 0.64. Since the detection was not very accurate, the Manhattan distance has a higher value than in the case of large aneurysms and SAHs (see second row of Figure 5.2).

In case of the small aneurysms the algorithm achieved the worst results. Dice coefficient equal to 0.09 is not very satisfying result. The reason of this is that there are cases, where patient has only one very small aneurysm. Therefore there is only a few true positive pixels to be segmented, so even a few small false positive segments

Tab. 5.1: Results of the full image segmentation and detection approach.

Metrics	All data	Small IAs	Large IAs and SAH
Dice	0.89 (0.04)	0.09 (0.04)	**0.90** (0.01)
Precision	0.90 (0.05)	0.05 (0.02)	0.96 (0.01)
Recall	0.89 (0.05)	0.29 (0.08)	0.85 (0.01)
PPV	**0.68** (0.46)	**0.68** (0.46)	**0.71** (0.42)
Sensitivity	**0.64** (0.46)	**0.40** (0.48)	**0.85** (0.32)
M. distance [px]	26.82 (45.04)	49.73 (54.62)	**13.20** (30.53)

can make a huge change in Dice coefficient. This is shown in Figure 5.3. On the other hand, segmentation of small IAs is comparable in PPV metric with the other two cases, thus there is similar number of false positive segments. Detection is also quite bad based on Sensitivity and Manhattan distance. This may be due to the presence of a large number of blood vessels, which tend to be segmented instead of the aneurysms.

5.1.2 Full image segmentation with elimination of false positive segments

As mentioned in Section 4.3.2 this approach uses the same U-net, that was discussed in Section 5.1.1. Thus, it has the same problems mainly in the case of small aneurysm detection. The difference of this approach is the effort to eliminate false positive segments, which was done by two methods.

The first method deals with elimination using an additional CNN described in the first part of Section 4.3.2. Results are presented in Table 5.2 and they do not differ very much from the results in Section 5.1.1 after rounding to two decimal places. Segmentation is still very good in terms of Dice coefficient. Since both, 17 FP and unfortunately 3 TP segments were eliminated, the value of PPV in case of all data is only 0.01 better. In case of small and large IAs the elimination is similar (eliminated were both, TP and FP segments) and therefore elimination of false positive segments is not very accurate with use of CNN. That is caused mainly, because it is difficult to train this kind of CNN to be very precise in classification of created segments. Even though the elimination is only small, Manhattan distance was improved a bit. Since the elimination of TP segments, the Sensitivity changed slightly, but after rounding to two decimal places the difference cannot be seen. The resulting detection is shown in second row of Figures 5.4 and 5.5.

The second method is fairly simple, but efficient. One image was segmented

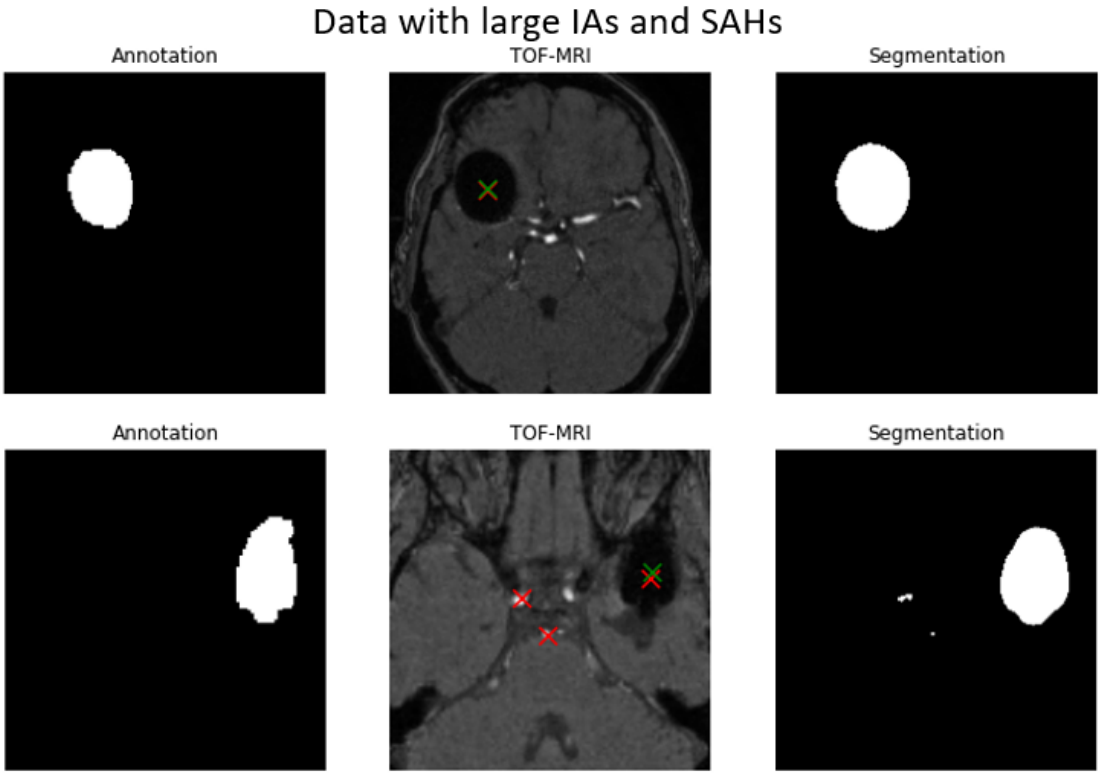

Fig. 5.1: This figure shows achieved detection using data with large aneurysms. A good segmentation and detection of large area is shown in the first row and a detection of a subarachnoid haemorrhage with a few false positive segments due to blood vessels is showns in the second row.

Tab. 5.2: Results of the full image segmentation and detection approach with elimination of false positive segments with use of CNN.

Metrics	**All data**	**Small IAs**	**Large IAs and SAH**
Dice	0.89 (0.04)	0.09 (0.04)	0.90 (0.01)
Precision	0.90 (0.05)	0.06 (0.02)	0.97 (0.01)
Recall	0.89 (0.05)	0.29 (0.08)	0.84 (0.02)
PPV	**0.69** (0.46)	**0.68** (0.46)	**0.70** (0.43)
Sensitivity	**0.64** (0.48)	**0.40** (0.52)	**0.85** (0.33)
M. distance [px]	25.26 (40.75)	44.23 (47.22)	13.18 (29.80)

several times with slightly different angle and subsequently an intersection of these images was made. Results are presented in Table 5.3. In case of a segmentation, the metrics differ only a little bit. In the case of all data, the elimination was successful as 641 false positive segments and only 8 true positive segments were eliminated

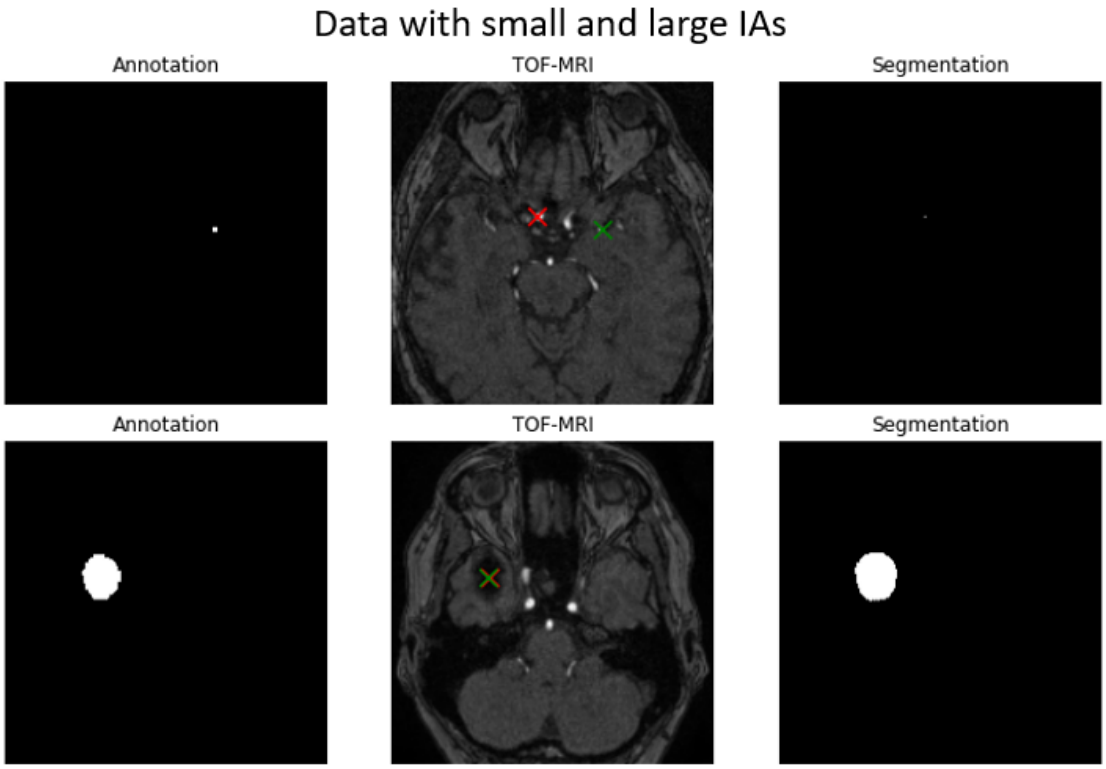

Fig. 5.2: This figure shows achieved detection using all data. The first row shows the main issue is segmentation of little parts of blood vessels and the second row shows a successful segmentation and detection of a small subarachnoid haemorrhage.

and therefore a value of PPV was increased. As the results show the elimination was similarly successful in both other cases (small IAs and large IAs). Due to the principle of this method, mostly small segments were eliminated, which is shown in the third row of both Figures 5.4 and 5.5. This, unfortunately, caused deterioration of Manhattan distance in case of small IAs and Sensitivity in case of all data, as there were more TP segments eliminated.

Comparison of these two elimination methods are shown in Figures 5.4 and 5.5. In the first row, there are images of approach from Section 5.1.1, the second row shows images of method using CNN and in the third row are images of the second elimination method presented. As discussed above, the second elimination method provides better results of PPV due to the elimination of small false positive segments. For example in last row of Figure 5.5 the PPV value was increased to value 1, as all the false positive segments were eliminated.

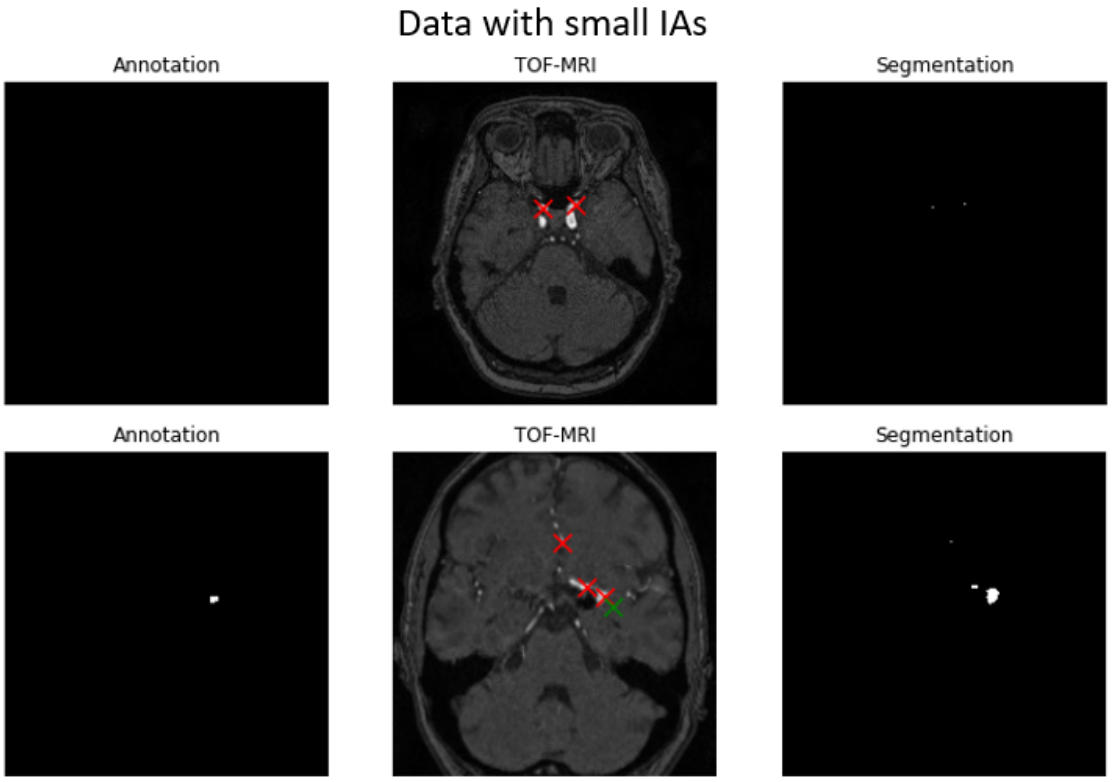

Fig. 5.3: This figure shows achieved detection using data with small aneurysms. There are two very small false positive segments in the first row and a segmentation and detection of a small aneurysm with a few FP segments in the second row.

Tab. 5.3: Results of the full image segmentation and detection approach with elimination of FP segments with use of intersection of images.

Metrics	**All data**	**Small IAs**	**Large IAs and SAH**
Dice	0.90 (0.04)	0.10 (0.04)	0.89 (0.00)
Precision	0.93 (0.05)	0.07 (0.03)	0.97 (0.00)
Recall	0.86 (0.05)	0.22 (0.06)	0.83 (0.01)
PPV	**0.84** (0.36)	**0.84** (0.37)	**0.82** (0.36)
Sensitivity	**0.60** (0.47)	**0.40** (0.52)	**0.85** (0.27)
M. distance [px]	26.88 (46.58)	**54.21** (67.37)	12.85 (30.04)

5.1.3 Image segmentation using patches

This approach was used because of the large disproportion of background pixels and aneurysm pixels. The main idea is to take the TOF-MRI image and divide it to smaller patches, segment these patches and reassemble the image back to the original state. This could not been done for training of the network and therefore

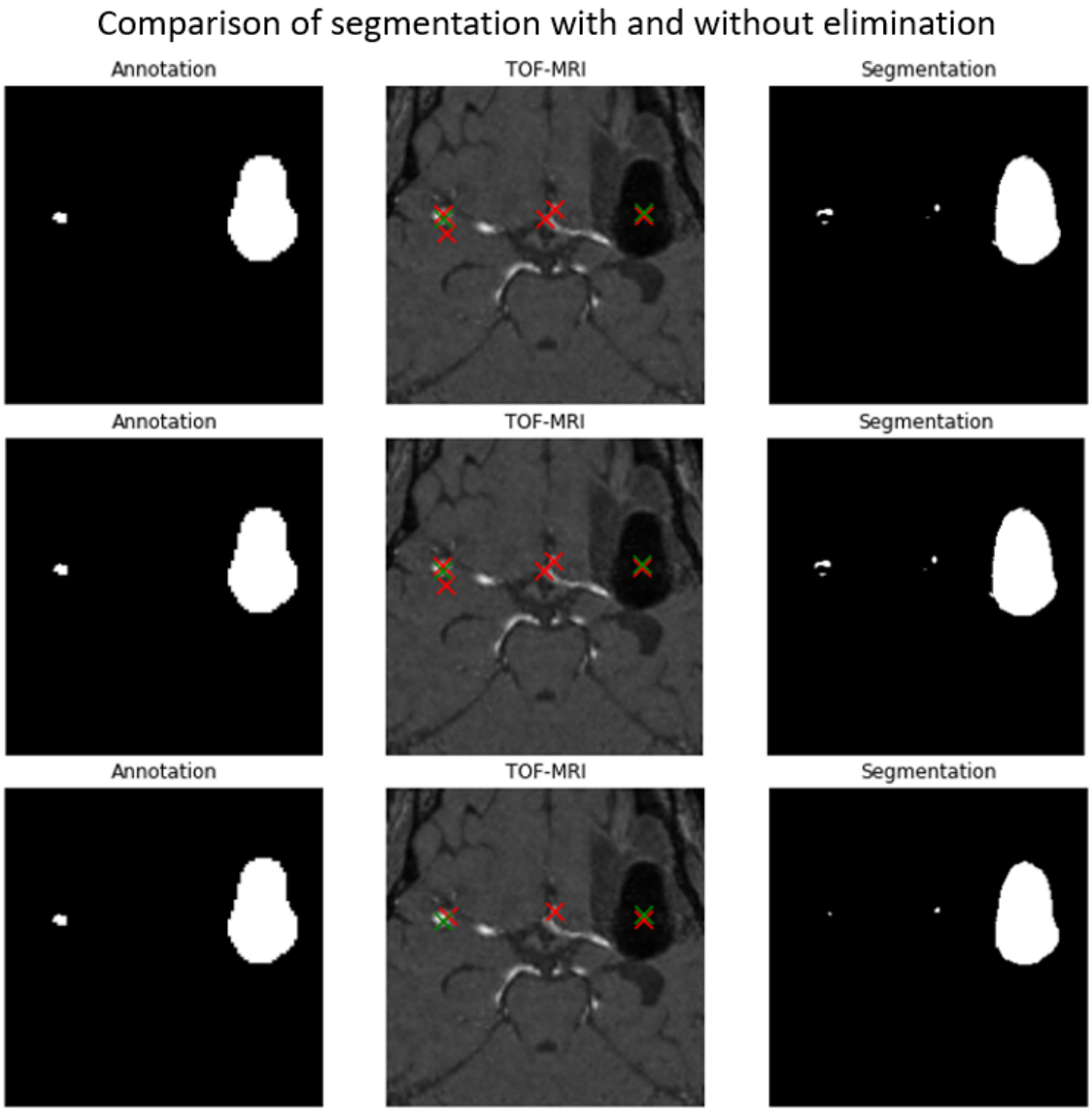

Fig. 5.4: This figure shows comparison of achieved detection without elimination (first row), with elimination with use of CNN (second row) and with use of the second method of elimination (last row). This is an example of data with large aneurysms and SAHs.

random patches were used as described in Section 4.3.3.

Results of evaluation on the random patches were only a bit worse, then in the full image approaches. For example, Dice coefficient was equal to 0.81 in case of all data, PPV was 0.86 and Manhattan distance had also good results (M. distance = 8.58). But in order to make the results comparable, they needed to be evaluated on images that had been disassembled, segmented and reassembled. These results are presented in Table 5.4. According to the results, the segmentation is not very accurate, as the Dice coefficient is only 0.56 for all validation data. However, in

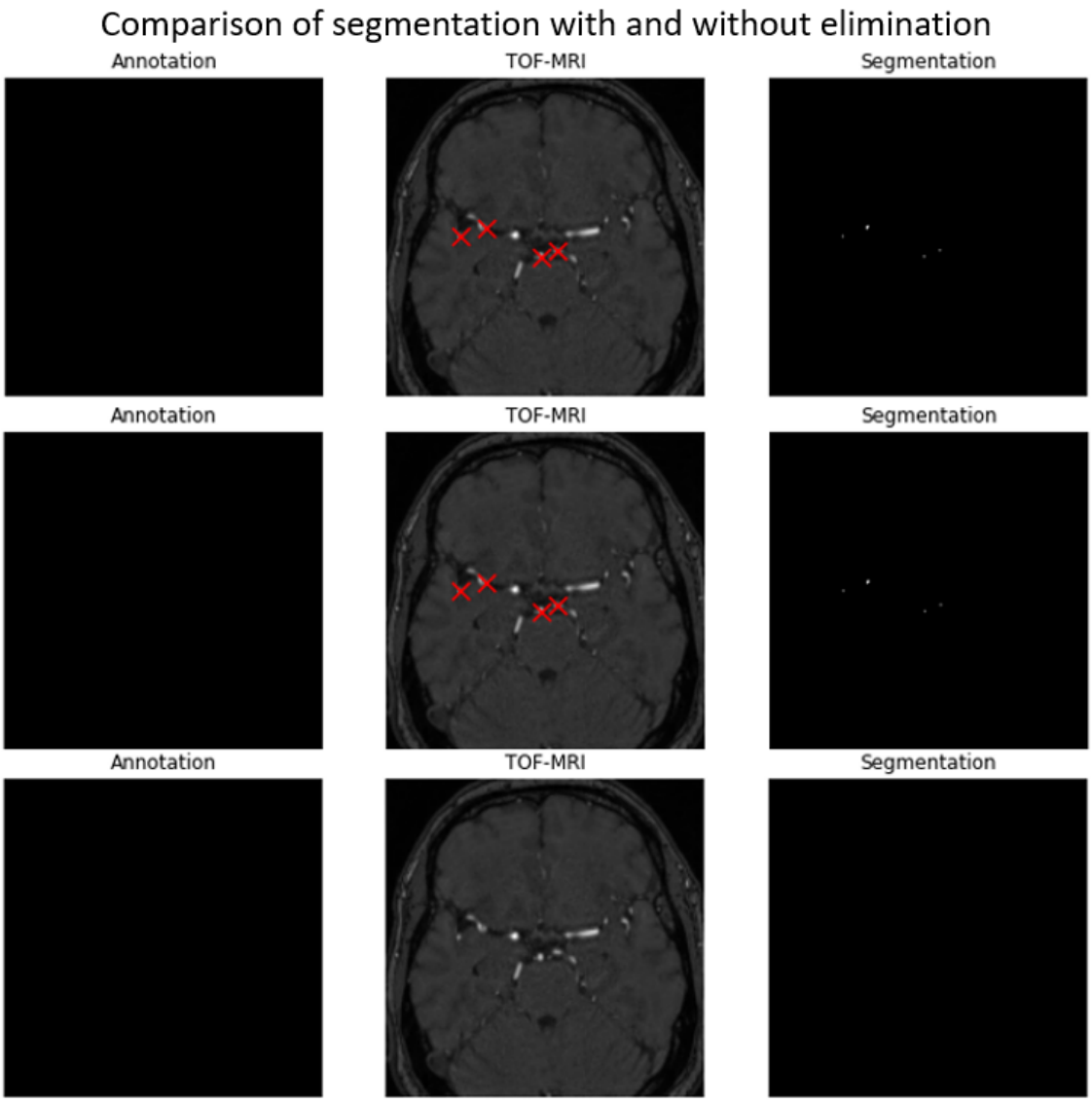

Fig. 5.5: This figure shows achieved detection using data with small IAs. It shows the difference of detection without any elimination of FP segments (first row), elimination with use of CNN (second row) and elimination using intersection of images (last row).

case of large IAs and SAH, the coefficient is much higher. One of the main issues of the segmentation problem is that large IAs and SAHs are divided and therefore inaccurately segmented when reassembled. This problem is shown in Figure 5.6.

Positive predictive value shows that there are a lot of false positive segments, which is shown in the first row of Figure 5.6. In case of small aneurysms, PPV is comparable with the other two cases, but the Dice coefficient and Precision are very low due to a high number of false positive segments. Even though the segmentation is not very accurate, some of centroids are still very precisely addressed according to

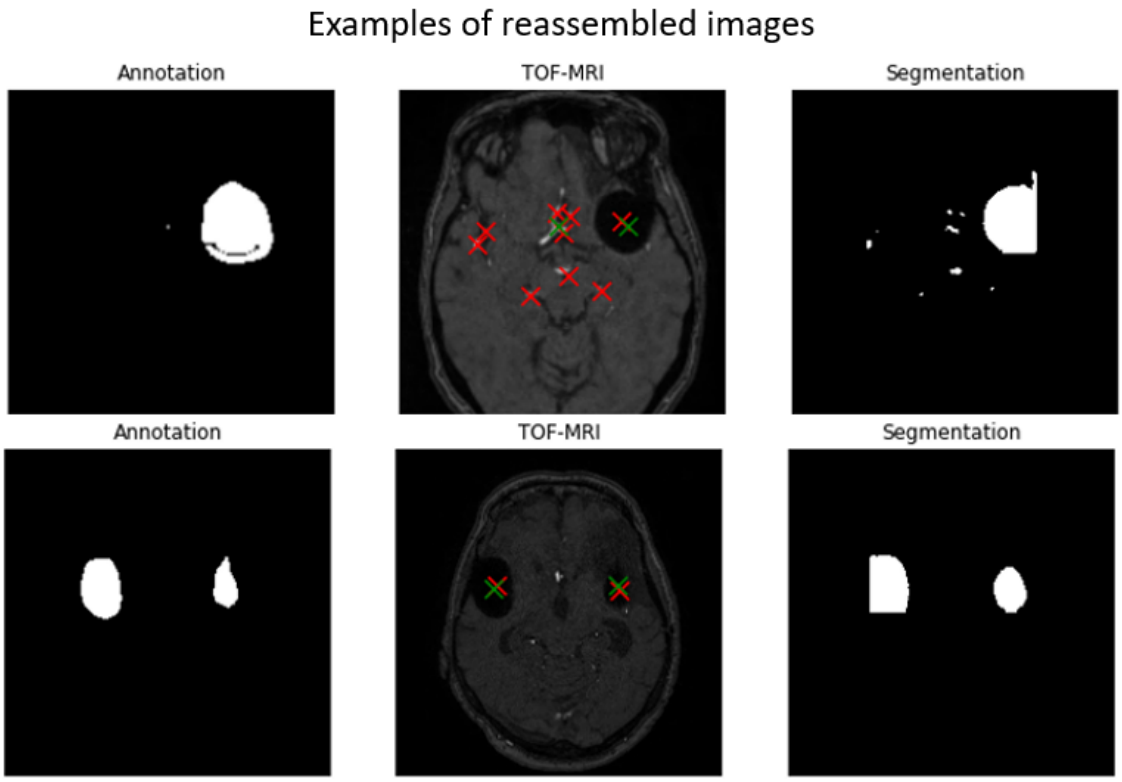

Fig. 5.6: This figure shows achieved detection using patched image approach. It shows case of segmentation and detection of a large amount of FP segments in the first row and an example of good detection of badly segmented aneurysms in the second row.

the Manhattan distance (see the second row of Figure 5.6). Sensitivity also confirms that detection is not bad in all three cases.

Tab. 5.4: Results of the patched image segmentation and detection approach.

Metrics	**All data**	**Small IAs**	**Large IAs and SAH**
Dice	**0.56** (0.07)	**0.03** (0.01)	**0.74** (0.05)
Precision	0.47 (0.06)	0.02 (0.00)	0.71 (0.06)
Recall	0.70 (0.08)	0.77 (0.14)	0.78 (0.05)
PPV	0.36 (0.47)	0.35 (0.47)	0.32 (0.41)
Sensitivity	**0.77** (0.47)	**0.58** (0.60)	**0.91** (0.25)
M. distance [px]	**14.78** (27.52)	33.94 (46.22)	6.56 (16.83)

As mentioned, the main problem in this approach was a large number of false positive segments. Therefore a method for elimination with use of intersection of images segmented under different angles was used. Results of this approach are

presented in Table 5.5. Segmentation has improved a bit according to Dice coefficient, however Recall has decreased due to a small cropping of the segments by intersection. Manhattan distance has increased a lot in case of all data, thus some of the segments, that were originally very close to the position of real aneurysms were eliminated. Images of this approach are shown in the first row of Figure 5.7, where a small difference can be seen in comparison with images in the second row. Another problem of the patched image approach were segments created far away from the region of interest (blood vessels), shown in second row of Figure 5.7, as well. Sensitivity has dropped a bit in all three cases due to elimination of some TP segments.

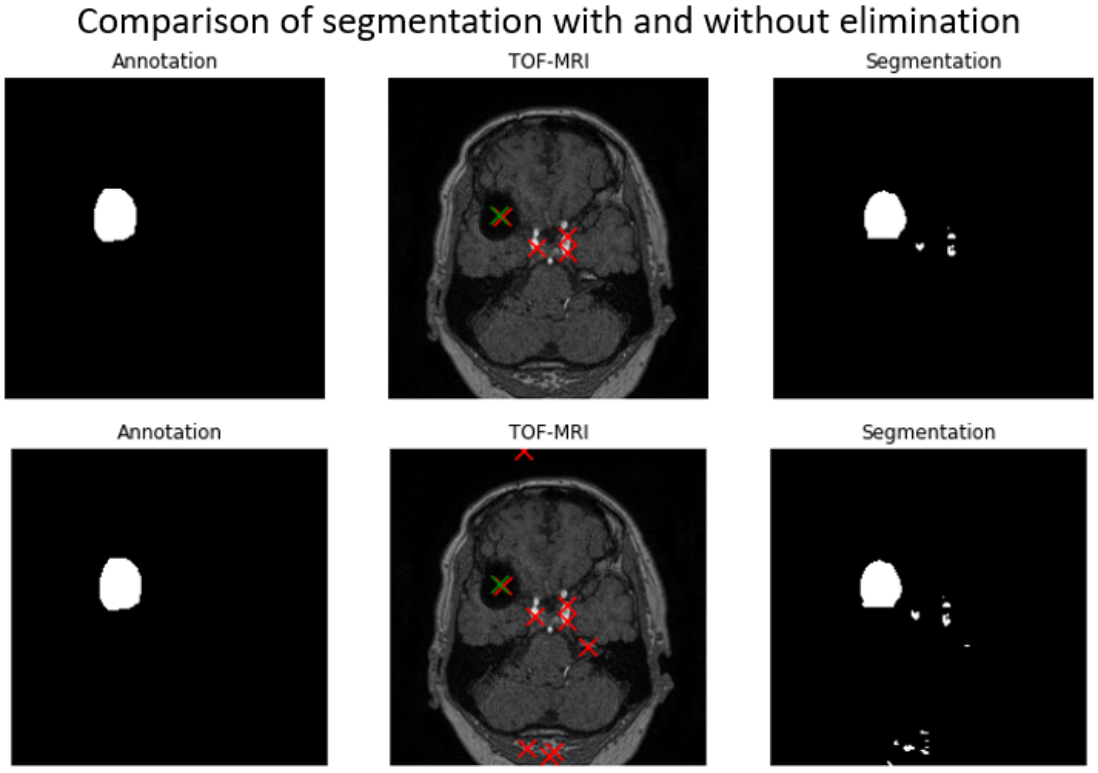

Fig. 5.7: This figure shows the difference between detection with elimination (first row) and detection without elimination of FP segments (second row).

5.1.4 3D image segmentation

All of the approaches already proposed in this thesis are implemented in 2D space, whereas this approach is in 3D space. It was proposed mainly because of the format of the available data, which is NIfTI, that is used to store images of brain obtained by MRI. Each case had several slices forming the whole 3D data. For the training of the 3D U-net it was important to work only with smaller amount of data, as there

Tab. 5.5: Results of the patched image segmentation and detection approach with elimination of the FP segments.

Metrics	All data	Small IAs	Large IAs and SAH
Dice	**0.60** (0.07)	**0.04** (0.01)	**0.76** (0.05)
Precision	0.54 (0.07)	0.02 (0.01)	0.76 (0.06)
Recall	**0.67** (0.08)	**0.70** (0.13)	**0.76** (0.05)
PPV	0.41 (0.49)	0.47 (0.49)	0.44 (0.44)
Sensitivity	**0.76** (0.43)	**0.54** (0.52)	**0.90** (0.26)
M. distance [px]	**43.22** (30.76)	29.90 (43.04)	7.15 (19.49)

was again a large number of background pixels. Therefore the net was trained only on smaller cubes of size $40 \times 40 \times 32$. More information about training is mentioned in Section 4.3.4.

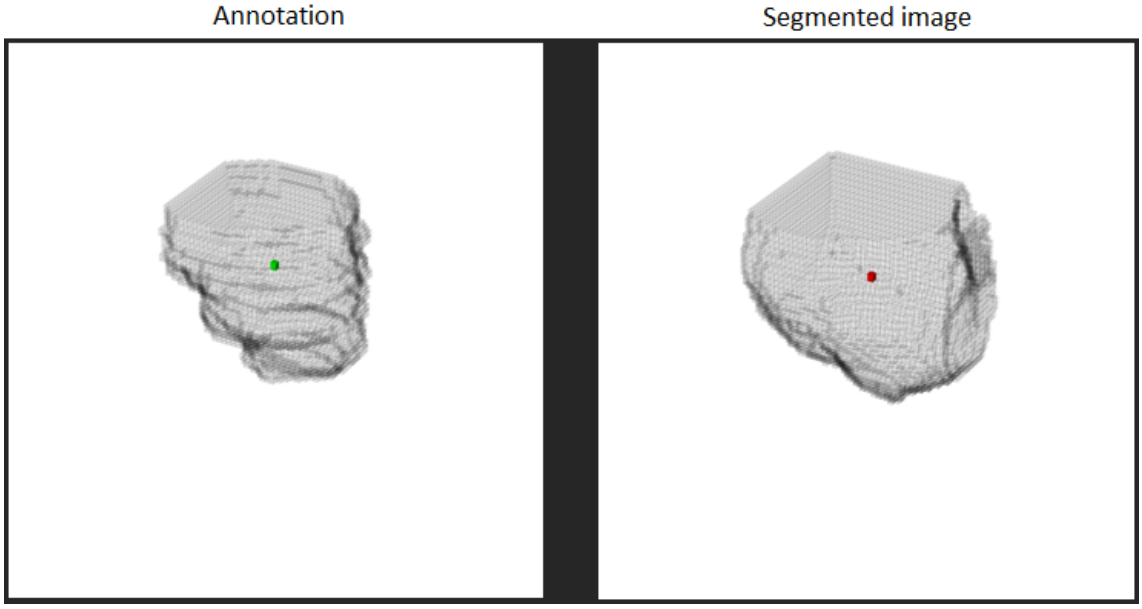

Fig. 5.8: This figure shows $40 \times 40 \times 32$ box segmentation of extensive subarachnoid haemorrhage using 3D U-net.

This 3D U-net was evaluated on both the small boxes and the reassembled data. In the first case, the U-net achieved on all available validation data a Dice coefficient equal to 0.69, Manhattan distance equal to 14.11, PPV equal to 0.63 and Sensitivity equal to 0.70. Based on these metrics the segmentation and detection does not perform very poorly, but it tends to create false positive segments, as well. Quite successful segmentation shown in Figure 5.8, where on the left, there is an annotation

and on the right is the segmented image.

Tab. 5.6: Results of the 3D segmentation and detection approach.

Metrics	All data	Small IAs	Large IAs and SAH
Dice	0.21 (0.05)	0.00 (0.00)	**0.49** (0.02)
Precision	0.13 (0.03)	0.00 (0.00)	0.36 (0.02)
Recall	0.55 (0.15)	0.09 (0.05)	0.76 (0.04)
PPV	**0.05** (0.01)	**0.01** (0.02)	**0.07** (0.04)
Sensitivity	**0.34** (0.63)	**0.21** (0.43)	**0.93** (0.25)
M. distance [px]	14.82 (12.01)	24.20 (20.85)	4.61 (2.63)

Results of reassembled data are presented in Table 5.6. The segmentation and therefore the subsequent detection is not very good in either case. The same problem occurs here as in the approach in Section 5.1.3, where subsequent merging of data into the original size leads to inaccurate segments. Furthermore, there are a lot of false positive segments according to the PPV values, in all three cases (all data, only small IAs, large IAs and SAHs). This large number of FP segments is also shown in Figure 5.9. This may be due to the fact that when segmenting a small cube, U-net tries to find segments that would not appear at all when segmenting the data as a whole. Sensitivity does not reach good values either, except in case of large IAs, where the Sensitivity is 0.93. However the positive predictive value, in this case, is only 0.07 and thus the detection is not successful, either.

5.2 Comparison of all used approaches

All approaches that were evaluated above in Section 5.1 will be compared with each other as well as with those of other authors, in this section. Results that will be compared are shown in Graphs 5.10, 5.13. According to the Graph 5.10 PPV can be said to follow Dice coefficient, therefore the bigger the Dice coeff., the bigger PPV and vice versa. This means that if false positive segments are removed, Dice coefficient should grow and therefore detection should be more precise.

That is why two elimination methods were proposed. First that uses small convolutional network, which decides which segment is removed. This method does not really make a big difference, because the shape of false positive and true positive segments does not differ much. Thus the network has learned to recognize some segments, but clearly not enough to make a big leap in improvement. However, with the second method, the difference is already visible in both full image and patched image approaches. These methods are compared in Figure 5.11 that shows

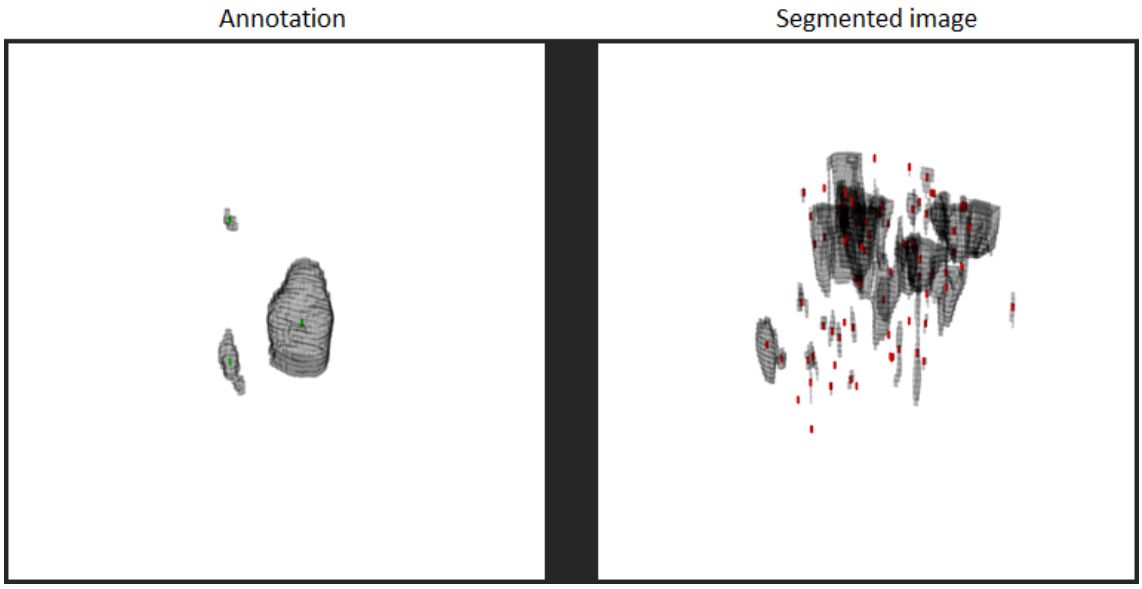

Fig. 5.9: This figure shows segmentation of SAH and one small aneurysm using 3D U-net.

better results achieved by the second elimination method by eliminating most of the FP segments. In this figure, red circles represent false positive segments, green circles represent true positive segments.

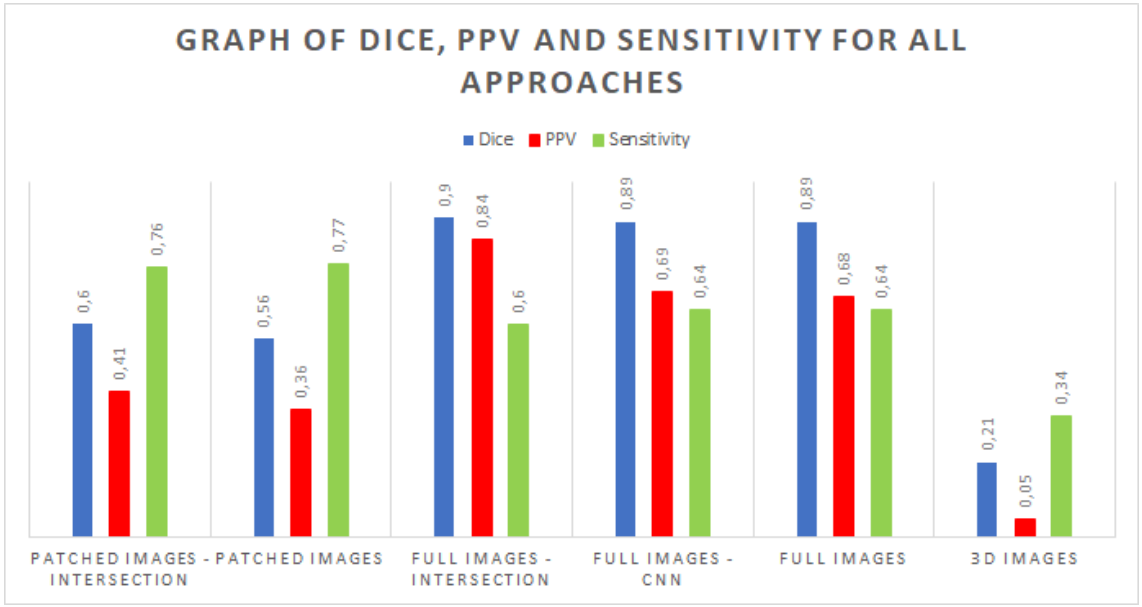

Fig. 5.10: Graph that compares values of Dice coefficient, Positive predictive value and Sensitivity of all approaches.

Another problem was a large amount of background pixels therefore the patched approach was suggested. As mentioned in 4.3.3 authors of [33] achieved Dice coef-

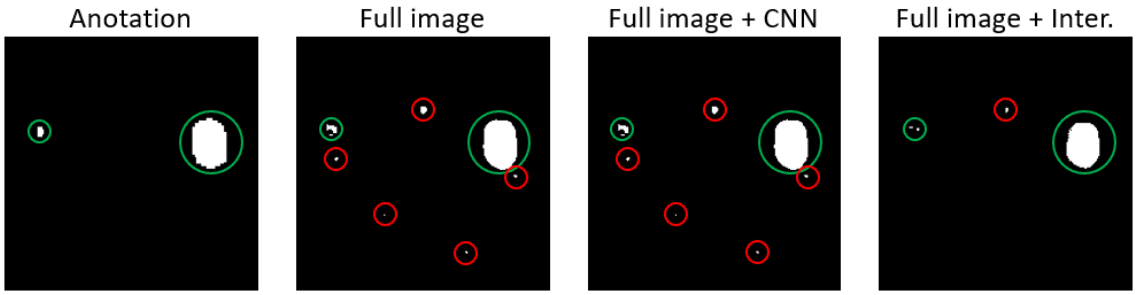

Fig. 5.11: This figure shows the difference, between methods proposed for elimination of false positive segments in segmented images.

ficient 0.90 using patches of images. However, in these TOF-MRI data the U-net had several problems with segmentation. There are falsely segmented blood vessels and structures far away from region of interest and therefore the PPV value is low, which is shown in the Graph 5.10, as well. So it seems that it is more appropriate to use full image approach with a loss function that can weight a positive response.

A 3D segmentation approach was proposed, as well. This approach had also issues with the ratio of the number of background pixels to the number of aneurysm pixels. Thus the method segments patches of $40 \times 40 \times 32$ and then the 3D image is reassembled from these patches. The main issue is the number of false positive segments again (see Figure 5.9), therefore the results are very poor, which is shown in the Graph 5.10, as well. This problem could be solved by one of the elimination methods, which is a very challenging task in 3D space.

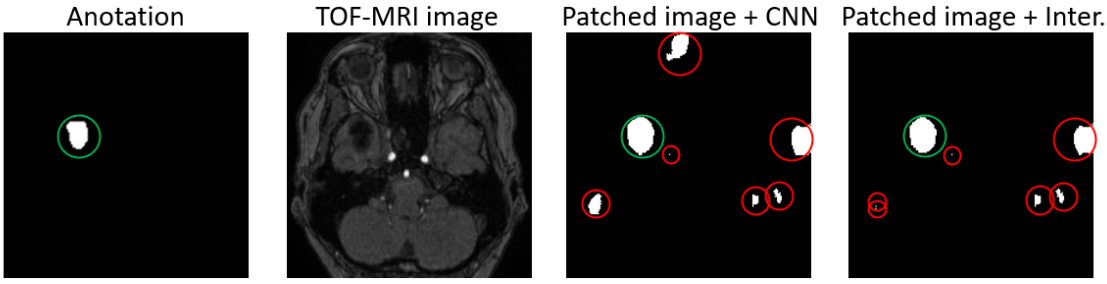

Fig. 5.12: This figure shows result of patched image approach and this approach with elimination of false positive segments.

The detection was highly dependent on the segmentation accuracy. Meaning that if there was a lot of false positive segments, the detection can be considered not very successful, even though the Manhattan distance might be low in some approaches. Boxplots of Manhattan distances of all approaches are shown in Graph 5.13. For example Manhattan distance is not very high in 3D segmentation approach, nevertheless according to the PPV value, which is very low, there are a lot of segments

that are not the real aneurysms. Sensitivity is important metric, too. It determines how many of the real aneurysms were really detected. So to evaluate the detection success rate, it is important to take all three of these metrics into account.

Thus, if we consider all of these metrics, it is very hard to determine the best approach. According to Sensitivity only, the best results are achieved by the segmentation using patches of images with elimination of FP segments. However, full image approach with elimination of FP segments using intersection of a few segmented images under a different angle has the best results in PPV value. That means, there is not as many correctly detected aneurysms as in the other method, but there is also much less false positive segments. So in the sense of detection, it is possible to say that the patched image method with elimination is better, however additional elimination method would have to be used, which would be able to remove a large number of those FP segments and thus increase the PPV.

The 3D segmentation approach has problem with false positive segments, as well. Even though, Manhattan distance is not as high as in the Full image approach, according to PPV value (less than 0.5 in all cases), there are a lot of segments that should not be present.

The calculation of the centroid was dependent on contour detection, and therefore influenced the results. The contours were not always obtained perfectly and so the centroid position was not always calculated correctly. In some cases, the centroid was not calculated at all. An example of such problem is shown in the second row of Figure 5.7. In the lower part of the images, there are segments that are not detected. On the contrary, in the upper part, there is a detected segment, that is not present in the image at all. Unfortunately, even after changing the method of obtaining the contours, the problem was not solved.

Compared to other authors who were dealing with aneurysm detection, the results of this thesis are slightly worse. The results are shown in the Table 5.7, where the best result achieved in this thesis are presented under the line in the last two rows of the table. The authors of the paper who are in the table in the first row ([29]) used a 3D segmentation neural network with DeepMedic architecture for detection. They do not report exactly how they performed the subsequent detection, but they achieved very good results, namely 0.9 Sensitivity. The authors mentioned in the second line also achieved a very high Sensitivity value. Their machine learning model is based on the untrained ResNet-18. To train their model, they had a significantly larger dataset, which they describe in more detail in their paper.

While the authors of the [34] paper mentioned in the third line achieved a Sensitivity of 0.7, the number of FP segments is only 0.26 per case, which is very good result. Their approach is based on a CNN classifier that works just with a volume of interest (VOI) and classifies whether a voxel belongs to an aneurysm or not. In

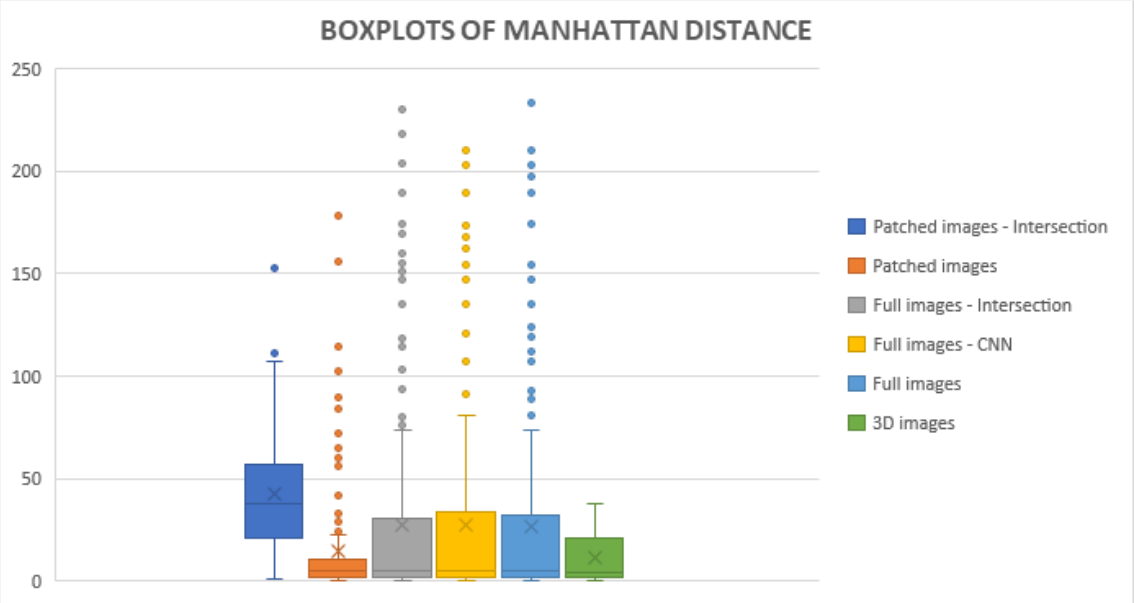

Fig. 5.13: Boxplots of Manhattan distances of all approaches. Boxes define the first and third quartiles, vertical lines show the variability of the data from these quartiles. Crosses represent the mean value, horizontal lines in the boxes represent median and dots are outlying values.

Tab. 5.7: Overview of results of other authors, dealing with aneurysm detection.

Authors	**Sensitivity**
A. Faron, T. Sichtermann and others [29]	0.90
D. Ueda, A. Yamamoto and others [28]	0.91-0.93
T. Nakao, S. Hanaoka and others [34]	0.70
K. M. Timmins, I. C. van der Schaaf and others [35]	0.02 - 0.70
Approach using patches of image with CNN elimination	0.77
Approach using 3D segmentation	0.34

the last row of Table 5.7 there is a paper, that summarises results of participants of ADAM challenge 2020. There are many approaches that used 3D U-net for segmentation. Furthermore there is one very interesting approach based on three 2D U-nets, that segment images in three different axis. The resulting image is created as a combination of segmented images from these three axes.

In summary, when compared to the methods of other authors, there is certainly room for many improvements and further experiments that could lead to better results. The first thing to do would be to improve the accuracy of segmentation. For example, by using a different network architecture or a combination of multiple

approaches, as other authors who participated in the ADAM challenge did. Furthermore, certainly the elimination of FP segments, which was a large problem in this thesis. This could be solved by other architectures, but also perhaps the use of other loss functions in training the U-net. Yet another possibility could be, for example, the detection of aneurysms only in the vicinity of blood vessels. Thus, it would be necessary to first obtain the areas of only these vessels and then search for aneurysms.

Conclusion

This thesis deals with the problem of detection of intracranial aneurysms from TOF-MRI angiographic images. The aim was to get acquainted with the problem, to create a literature research and then to apply the methods from the theory part in practical aneurysm detection. The theory part of this thesis discusses intracranial aneurysms, their diagnosis and treatment. Furthermore, classical methods of intracranial aneurysm detection and machine learning based methods are presented, as well.

Among the mentioned machine learning methods, U-net neural network was chosen to solve the segmentation problem whose output is a probabilistic map. This map was subsequently thresholded to produce a binary image where segments representing potential anuerysms were detected. The detection was performed by calculating the centroid of these segments with use of their contours. Two issues in particular were addressed in the segmentation task. A large disproportion between the number of background pixels and aneurysm pixels and furthermore the problem of generating a large number of false positive segments. For these reasons, several segmentation approaches and modifications have been proposed in this thesis.

At the end of the practical part is an evaluation of the different approaches. Several statistical metrics were used for the evaluation. Precision, Recall and Dice coefficient were selected for the segmentation task. Subsequent detection was evaluated based on positive predictive value (PPV), Manhattan distance and Sensitivity. The best results of detection is difficult to determine. The approach using patches of images with subsequent elimination of FP segments achieved good results. In this case, the elimination was performed by intersecting images that were repeatedly segmented at slightly different angles. The approach achieves a Dice coefficient of 0.6 and PPV of 0.41, however it achieved the best Sensitivity of 0.76. On the other hand, Full image segmentation with the same elimination of FP segments achieved worse Sensitivity of 0.60, but the PPV is equal to 0.84. In case of 3D segmentation approach, there is a problem with number of FP segments and the Sensitivity is not very good either, even though Manhattan distance is very low.

When comparing the results with other authors, there is some room for improvement. For example, it would be possible to try other network architectures or combination of several approaches.

Bibliography

[1] GASPAROTTI, Roberto a Roberto LISERRE. Intracranial aneurysms. European Radiology [online]. 2005, 15(3), 441-447 [cit. 2021-11-27]. ISSN 0938-7994. doi:10.1007/s00330-004-2614-8. Available from: Online reference

[2] CARANCI, F., F. BRIGANTI, L. CIRILLO, M. LEONARDI a M. MUTO. Epidemiology and genetics of intracranial aneurysms. European Journal of Radiology [online]. 2013, 82(10), 1598-1605 [cit. 2021-11-27]. ISSN 0720048X. doi:10.1016/j.ejrad.2012.12.026. Online reference

[3] SHAH, Rahul S. a Deva S. JEYARETNA. Cerebral vascular anatomy and physiology. Surgery (Oxford) [online]. 2021, 39(8), 463-469 [cit. 2021-11-27]. ISSN 02639319. doi:10.1016/j.mpsur.2021.06.006. Available from: Online reference

[4] WILLIE, Christopher K., Yu-Chieh TZENG, Joseph A. FISHER a Philip N. AINSLIE. Integrative regulation of human brain blood flow. The Journal of Physiology [online]. 2014, 592(5), 841-859 [cit. 2021-11-27]. ISSN 00223751. doi:10.1113/jphysiol.2013.268953. Available from: Online reference

[5] WILLIE, C. K., D. B. MACLEOD, A. D. SHAW, et al. Regional brain blood flow in man during acute changes in arterial blood gases. The Journal of Physiology [online]. 2012, 590(14), 3261-3275 [cit. 2021-11-28]. ISSN 00223751. doi:10.1113/jphysiol.2012.228551. Available from: Online reference

[6] BAIN, Anthony R., Kurt J. SMITH, Nia C. LEWIS, Glen E. FOSTER, Kevin W. WILDFONG, Christopher K. WILLIE, Geoffrey L. HARTLEY, Stephen S. CHEUNG a Philip N. AINSLIE, 2013. Regional changes in brain blood flow during severe passive hyperthermia: effects of PaCO2 and extracranial blood flow [online]. 1. září 2013. B.m.: American Physiological Society. doi:10.1152/japplphysiol.00394.2013. Available from: Online reference

[7] LIANG, X., Q. ZOU, Y. HE a Y. YANG. Coupling of functional connectivity and regional cerebral blood flow reveals a physiological basis for network hubs of the human brain. Proceedings of the National Academy of Sciences [online]. 2013, 110(5), 1929-1934 [cit. 2021-11-28]. ISSN 0027-8424. doi:10.1073/pnas.1214900110. Available from: Online reference

[8] WANG, Yutang, Theophilus I. EMETO, James LEE, Laurence MARSHMAN, Corey MORAN, Sai-wang SETO a Jonathan GOLLEDGE. Mouse Models of Intracranial Aneurysm. Brain Pathology [online]. 2015, 25(3), 237-247 [cit. 2021-11-28]. ISSN 10156305. doi:10.1111/bpa.12175. Available from: Online reference

[9] CHALOUHI, Nohra, Muhammad S ALI, Pascal M JABBOUR, Stavropoula I TJOUMAKARIS, L Fernando GONZALEZ, Robert H ROSENWASSER, Walter J KOCH a Aaron S DUMONT. Biology of Intracranial Aneurysms: Role of Inflammation. Journal of Cerebral Blood Flow and Metabolism [online]. 2012, 32(9), 1659-1676 [cit. 2021-11-28]. ISSN 0271-678X. doi:10.1038/jcbfm.2012.84. Available from: Online reference

[10] HACEIN-BEY, Lotfi a James M. PROVENZALE. Current Imaging Assessment and Treatment of Intracranial Aneurysms. American Journal of Roentgenology [online]. 2011, 196(1), 32-44 [cit. 2021-11-28]. ISSN 0361-803X. doi:10.2214/AJR.10.5329. Available from: Online reference

[11] CHEN, Wenhua, Yilin YANG, Wei XING, Jianguo QIU a Ya PENG. Application of multislice computed tomographic angiography in diagnosis and treatment of intracranial aneurysms. Clinical Neurology and Neurosurgery [online]. 2010, 112(7), 563-571 [cit. 2021-11-28]. ISSN 03038467. doi:10.1016/j.clineuro.2010.04.022. Available from: Online reference

[12] WEISHAUPT, Dominik, Victor D. KOCHLI a Borut MARINCEK. How Does MRI Work?: An Introduction to the Physics and Function of Magnetic Resonance Imaging. Second Edition. Berlin: Springer-Verlag Berlin Heidelberg, 2008. ISBN 978-3540300670.

[13] Intracranial Vascular Malformations and Aneurysms [online]. Berlin/Heidelberg: Springer-Verlag, 2006 [cit. 2021-12-05]. Medical Radiology. ISBN 3-540-26250-4. doi:10.1007/3-540-30002-3. Available from: Online reference

[14] CARR, James C. a Timothy J. CARROLL, ed. Magnetic Resonance Angiography [online]. New York, NY: Springer New York, 2012 [cit. 2021-12-05]. ISBN 978-1-4419-1685-3. doi:10.1007/978-1-4419-1686-0. Available from: Online reference

[15] WEBSTER, John G. Medical Instrumentation: Application and Design. Fourth Edition. USA: John Wiley and Sons, 2009. ISBN 978-0-471-67600-3.

[16] PRADILLA, Gustavo, Robert T. WICKS, Uri HADELSBERG, Philippe GAILLOUD, Alexander L. COON, Judy HUANG a Rafael J. TAMARGO. Accuracy of Computed Tomography Angiography in the Diagnosis of Intracranial Aneurysms. World Neurosurgery [online]. 2013, 80(6), 845-852 [cit. 2021-11-30]. ISSN 18788750. doi:10.1016/j.wneu.2012.12.001. Available from: Online reference

[17] PANDEY, Shilpa, Michael HAKKY, Ellie KWAK, Hernan JARA, Carl A. GEYER a Sami H. ERBAY. Application of Basic Principles of Physics to Head and Neck MR Angiography: Troubleshooting for Artifacts. RadioGraphics [online]. 2013, 33(3), E113-E123 [cit. 2021-12-05]. ISSN 0271-5333. doi:10.1148/rg.333125148. Available from: Online reference

[18] SCHOFIELD, R., L. KING, U. TAYAL, I. CASTELLANO, J. STIRRUP, F. PONTANA, J. EARLS a E. NICOL. Image reconstruction: Part 1 – understanding filtered back projection, noise and image acquisition. Journal of Cardiovascular Computed Tomography [online]. 2020, 14(3), 219-225 [cit. 2021-12-05]. ISSN 19345925. doi:10.1016/j.jcct.2019.04.008. Available from: Online reference

[19] CASTILLO, Mauricio. Digital Subtraction Angiography (DSA): Basic Principles. RAMALHO, Joana N. a Mauricio CASTILLO, ed. Vascular Imaging of the Central Nervous System [online]. Oxford, UK: John Wiley and Sons, 2014, 2013-11-30, s. 207-220 [cit. 2021-12-05]. ISBN 9781118434550. doi:10.1002/9781118434550.ch14. Available from: Online reference

[20] VIKRAM, K. and S. PADMAVATHI. Facial parts detection using Viola Jones algorithm. In: 2017 4th International Conference on Advanced Computing and Communication Systems (ICACCS) [online]. IEEE, 2017, 2017, s. 1-4 [cit. 2021-12-11]. ISBN 978-1-5090-4559-4. doi:10.1109/ICACCS.2017.8014636. Available from: Online reference

[21] SHU, Chang, Xiaoqing DING and Chi FANG. Histogram of the oriented gradient for face recognition. Tsinghua Science and Technology [online]. 2011, 16(2), 216-224 [cit. 2021-12-11]. ISSN 1007-0214. doi:10.1016/S1007-0214(11)70032-3. Available from: Online reference

[22] TANG, Yuxing, Xiaofang WANG, Emmanuel DELLANDREA and Liming CHEN. Weakly Supervised Learning of Deformable Part-Based Models for Object Detection via Region Proposals. IEEE Transactions on Multimedia [online]. 2017, 19(2), 393-407 [cit. 2021-12-11]. ISSN 1520-9210. doi:10.1109/TMM.2016.2614862. Available from: Online reference

[23] ZHAO, Zhong-Qiu, Peng ZHENG, Shou-Tao XU a Xindong WU. Object Detection With Deep Learning: A Review. IEEE Transactions on Neural Networks and Learning Systems [online]. 2019, 30(11), 3212-3232 [cit. 2021-12-12]. ISSN 2162-237X. doi:10.1109/TNNLS.2018.2876865. Available from: Online reference

[24] LIU, Yang, Peng SUN, Nickolas WERGELES a Yi SHANG. A survey and performance evaluation of deep learning methods for small object detection. Expert Systems with Applications [online]. 2021, 172 [cit. 2021-12-12]. ISSN 09574174. doi:10.1016/j.eswa.2021.114602. Available from: Online reference

[25] DU, Getao, Xu CAO, Jimin LIANG, Xueli CHEN a Yonghua ZHAN. Medical Image Segmentation based on U-Net: A Review. Journal of Imaging Science and Technology [online]. 2020, 64(2), 20508-1-20508-12 [cit. 2021-12-12]. ISSN 1062-3701. doi:10.2352/J.ImagingSci.Technol.2020.64.2.020508. Available from: Online reference

[26] RONNEBERGER, Olaf, Philipp FISCHER a Thomas BROX. U-Net: Convolutional Networks for Biomedical Image Segmentation. NAVAB, Nassir, Joachim HORNEGGER, William M. WELLS a Alejandro F. FRANGI, ed. Medical Image Computing and Computer-Assisted Intervention – MICCAI 2015 [online]. Cham: Springer International Publishing, 2015, 2015-11-18, s. 234-241 [cit. 2021-12-19]. Lecture Notes in Computer Science. ISBN 978-3-319-24573-7. doi:10.1007/978-3-319-24574-4_28. Available from: Online reference

[27] DONG, Hao, Guang YANG, Fangde LIU, Yuanhan MO a Yike GUO. Automatic Brain Tumor Detection and Segmentation Using U-Net Based Fully Convolutional Networks. VALDÉS HERNÁNDEZ, María a Víctor GONZÁLEZ-CASTRO, ed. Medical Image Understanding and Analysis [online]. Cham: Springer International Publishing, 2017, 2017-06-22, s. 506-517 [cit. 2021-12-19]. Communications in Computer and Information Science. ISBN 978-3-319-60963-8. doi:10.1007/978-3-319-60964-5_44. Available from: Online reference

[28] UEDA, Daiju, Akira YAMAMOTO, Masataka NISHIMORI, et al. Deep Learning for MR Angiography: Automated Detection of Cerebral Aneurysms. Radiology [online]. 2019, 290(1), 187-194 [cit. 2021-12-26]. ISSN 0033-8419. doi:10.1148/radiol.2018180901. Available from: Online reference

[29] FARON, Anton, Thorsten SICHTERMANN, Nikolas TEICHERT, et al. Performance of a Deep-Learning Neural Network to Detect Intracranial Aneurysms from 3D TOF-MRA Compared to Human Readers. Clinical Neuroradiology [online]. 2020, 30(3), 591-598 [cit. 2021-12-26]. ISSN 1869-1439. doi:10.1007/s00062-019-00809-w. Available from: Online reference

[30] YANG, Xi, Ding XIA, Taichi KIN a Takeo IGARASHI. A Two-step Surface-based 3D Deep Learning Pipeline for Segmentation of Intracranial Aneurysms [online]. 2020, , 1-9 [cit. 2021-12-26]. Available from: https://arxiv.org/abs/2006.16161

[31] ÇIÇEK, Özgün, Ahmed ABDULKADIR, Soeren S. LIENKAMP, Thomas BROX a Olaf RONNEBERGER. 3D U-Net: Learning Dense Volumetric Segmentation from Sparse Annotation. OURSELIN, Sebastien, Leo JOSKOWICZ, Mert R. SABUNCU, Gozde UNAL a William WELLS, ed. Medical Image Computing and Computer-Assisted Intervention – MICCAI 2016 [online]. Cham: Springer International Publishing, 2016, 2016-10-02, s. 424-432 [cit. 2022-04-16]. Lecture Notes in Computer Science. ISBN 978-3-319-46722-1. doi:10.1007/978-3-319-46723-8_49. Available from: Online reference

[32] ATABAY, Habibollah. Binary shape classification using Convolutional Neural Networks. The IIOAB Journal [online]. 2016, October 2016, 7, 332-336 [cit. 2022-04-17]. Available from: Online reference

[33] BEN NACEUR, Mostefa, Mohamed AKIL, Rachida SAOULI a Rostom KACHOURI. Fully automatic brain tumor segmentation with deep learning-based selective attention using overlapping patches and multi-class weighted cross-entropy. Medical Image Analysis [online]. 2020, 63 [cit. 2022-03-13]. ISSN 13618415. doi:10.1016/j.media.2020.101692. Available from: Online reference

[34] NAKAO, Takahiro, Shouhei HANAOKA, Yukihiro NOMURA, et al. Deep neural network-based computer-assisted detection of cerebral aneurysms in MR angiography. Journal of Magnetic Resonance Imaging [online]. 2018, 47(4), 948-953 [cit. 2022-05-08]. ISSN 1053-1807. doi:10.1002/jmri.25842- Available from: Online reference

[35] TIMMINS, Kimberley M., Irene C. VAN DER SCHAAF, Edwin BENNINK, et al. Comparing methods of detecting and segmenting unruptured intracranial aneurysms on TOF-MRAS: The ADAM challenge. NeuroImage [online]. 2021, 238 [cit. 2022-05-08]. ISSN 10538119. doi:10.1016/j.neuroimage.2021.118216. Available from: Online reference

[36] VAN DER WALT, Stéfan, Johannes L. SCHÖNBERGER, Juan NUNEZ-IGLESIAS, François BOULOGNE, Joshua D. WARNER, Neil YAGER, Emmanuelle GOUILLART a Tony YU. Scikit-image: image processing in Python. PeerJ [online]. 2014, 2 [cit. 2022-05-15]. ISSN 2167-8359. doi:10.7717/peerj.453. Available from: Online reference

Symbols and abbreviations

IA	Intracranial aneurysm
SAH	Subarachnoid haemorrhage
CT	Computer tomography
CTA	Computer tomography angiography
DSA	Digital subtraction angiography
MRI	Magnetic resonance imaging
MRA	Magnetic resonance angiography
TOF	Time of flight
TP, FP, TN	True positive, false positive, true negative
PPV	Positive predictive value
TR	Repetition time
TE	Echo time
SE	Spin echo
IR	Inversion recovery
STIR	Short time inversion recovery
FLAIR	Fluid-attenuated inversion recovery
GRE	Gradient echo
HOG	Histogram of Oriented Gradients
DPM	Deformable part-baset Model
SVM	Support vector machine
VOI	Volume of interest